

An improved measurement of the flux distribution of the Ly α forest in QSO absorption spectra: the effect of continuum fitting, metal contamination and noise properties^{*}

T.-S. Kim^{1,2}, J. S. Bolton^{2,3}, M. Viel^{2,4}, M. G. Haehnelt², R. F. Carswell²

¹ *Astrophysikalisches Institut Potsdam, An der Sternwarte 16, D-14482 Potsdam, Germany*

² *Institute of Astronomy, Madingley Road, Cambridge CB3 0HA, UK*

³ *Max-Planck-Institut für Astrophysik, Karl-Schwarzschild-Str. 1, 85748 Garching bei München, Germany*

⁴ *INAF-Osservatorio Astronomico di Trieste, Via G. B. Tiepolo 11, I-34131 Trieste, Italy*

Received 2007 July 7; Accepted 2007 September 3

ABSTRACT

We have performed an extensive Voigt profile analysis of the neutral hydrogen (H I) and metal absorption present in a sample of 18 high resolution, high signal-to-noise QSO spectra observed with VLT/UVES. We use this analysis to separate the metal contribution from the H I absorption and present an improved measurement of the flux probability distribution function (PDF) due to H I absorption alone at $\langle z \rangle = 2.07$, 2.52, and 2.94. The flux PDF is sensitive to the continuum fit in the normalised flux range $0.8 < F < 1.0$ and to metal absorption at $0.2 < F < 0.8$. Our new measurements of the flux PDF due to H I absorption alone are systematically lower at $0.2 < F < 0.8$ by up to 30% compared to the widely used measurement of McDonald et al. (2000), based on a significantly smaller sample of Keck/HIRES data. This discrepancy is probably due to a combination of our improved removal of the metal absorption and cosmic variance, since variations in the flux PDF between different lines-of-sight are large. The H I effective optical depth $\tau_{\text{H I}}^{\text{eff}}$ at $1.7 < z < 4$ is best fit with a single power law, $\tau_{\text{H I}}^{\text{eff}} = (0.0023 \pm 0.0007)(1+z)^{3.65 \pm 0.21}$, in good agreement with previous measurements from comparable data. As also found previously, the effect of noise on the flux distribution is not significant in high resolution, high signal-to-noise data.

Key words: cosmology: observations – intergalactic medium – quasars: absorption lines

1 INTRODUCTION

The Ly α forest refers to the numerous, narrow absorption features bluewards of the Ly α emission line in the spectra of high-redshift QSOs. Our understanding of the origin of the Ly α forest has made major progress with the advent of high resolution spectroscopy (Cowie et al. 1995; Hu et al. 1995; Lu et al. 1996; Kirkman & Tytler 1997; Rauch et al. 1997; Cristiani & D’Odorico 2000; Kim et al. 2001; Janknecht et al. 2006) and the availability of hydrodynamic cosmological simulations (Cen et al. 1994; Miralda-Escudé et al. 1996; Zhang et al. 1997; Weinberg et al. 1998; Croft et al. 1998; Theuns et al. 1998;

Bryan et al. 1999; Davé et al. 1999; Croft et al. 2002; Jena et al. 2005). Comparison of the predictions from hydrodynamic cosmological simulations with observations have established a picture where the Ly α forest is due to the neutral hydrogen (H I) component of the warm ($\sim 10^4$ K) photoionised intergalactic medium (IGM) which traces moderate-amplitude density fluctuations of the (dark) matter distribution in a simple manner. In this picture the spectra of high- z QSOs provide a one-dimensional probe of the matter density along the line-of-sight to high redshift QSOs. The flux distribution in QSO absorption spectra thus encodes information on the underlying matter distribution and evolution and the Ly α forest has been recognised as a powerful cosmological tool, complementing other cosmological probes.

So far it is mainly the power spectrum of the flux dis-

^{*} Based on data taken from ESO archive obtained with UVES at VLT, Paranal, Chile.

tribution which has been used to quantitatively probe the properties of the large scale distribution of matter and its dependence on cosmological parameters. The flux power spectrum is sensitive to the matter power spectrum over a wide redshift range ($2 < z < 4$) and on scales of $1\text{--}50 h^{-1}\text{Mpc}$, significantly smaller than those probed by CMB fluctuations, galaxy surveys and gravitational lensing (Croft et al. 2002; Seljak, McDonald & Makarov 2003; Viel, Haehnelt & Springer 2004b; McDonald et al. 2006; Viel, Haehnelt & Lewis 2006; Lesgourges et al. 2007).

The probability distribution of the flux is also sensitive to the spatial distribution of dark matter and cosmological parameters, in particular, the amplitude of matter fluctuations (Rauch et al. 1997; Weinberg et al. 1998; Theuns, Schaye & Haehnelt 2000; Meiksin, Bryan & Machacek 2001). However, the effect of the thermal state of the IGM (Theuns et al. 2000) and other uncertainties make it more difficult to extract this information from the flux PDF. First attempts at a joint analysis of the flux PDF and the flux power spectrum have been made (Desjacques & Nusser 2005; Lidz et al. 2006; Desjacques, Nusser & Sheth 2007). The analysis of Desjacques et al. gives a somewhat smaller amplitude for the matter power spectrum compared to studies based on the flux power spectrum alone. Note, however, that these results were based on dark-matter-only numerical simulations in which the gas distribution was modelled in an approximate way rather than on full hydrodynamical simulations.

The measured flux PDF is sensitive not only to the H I absorption, but also, unfortunately, to continuum level uncertainties, contaminating heavy element absorption, and noise. The effect of continuum fitting uncertainties on the H I effective optical depth has been discussed in detail (Press, Rybicki & Schneider 1993; Kim et al. 2002; Bernardi et al. 2003; Tytler et al. 2004; Kirkman et al. 2005), but their impact on the flux PDF has not been considered as extensively (see Rauch et al. 1997 and McDonald et al. 2000 for notable exceptions). Very little, if anything, has been done to quantify the effect of metal absorption and noise on the flux PDF. To remedy these omissions, we perform a detailed Voigt profile analysis of the metal and H I absorption in 18 high resolution, high signal-to-noise (S/N) VLT/UVES QSO absorption spectra to assess the impact of continuum fitting uncertainties, metal absorption, and noise properties on the H I flux probability distribution at $1.7 < z < 3.2$ and the H I effective optical depth at $1.7 < z < 4$.

Our study is based on a factor of two larger sample and probes towards lower z than similar work based on 8 Keck/HIRES spectra by McDonald et al. (2000). It also differs significantly in the way we perform the continuum fitting and, more importantly, in the level of the characterisation of metal absorption. Most previous estimates of the effective optical depth and the flux PDF due to H I absorption have either removed the metal lines *statistically* (Tytler et al. 2004; Kirkman et al. 2005), excluded the metal-contaminated regions from the study (McDonald et al. 2000; Lidz et al. 2006) or included absorption due to metal lines (Songaila 2004).

We have carefully identified and *fitted* metal and H I absorption lines with Voigt profiles for our sample of 18 spectra. The line fitting is essentially complete in the Ly α for-

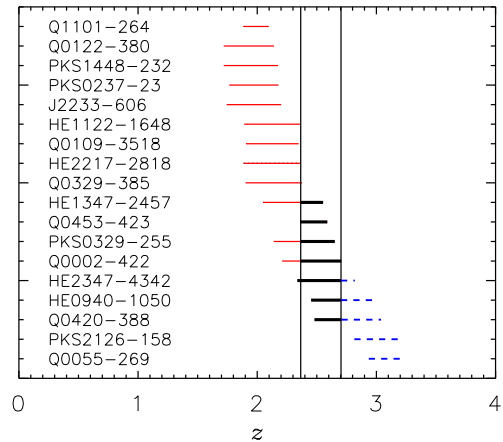


Figure 1. The redshift range of the Ly α forest in the spectra used for this study. The sample is divided into redshift bins. The thin dotted lines, thick solid lines and dashed lines represent the $\langle z \rangle = 2.07$, $\langle z \rangle = 2.52$ and $\langle z \rangle = 2.94$ sub-sample, respectively.

est region and redwards of the Ly α emission lines, but less complete in the higher-order Lyman forest where the corresponding spectral regions were not always available. During the fitting process, we have adjusted the initially estimated continuum level by a localised continuum fit in order to get an overall satisfactory fit to multiple-transition metal lines and higher-order Lyman series lines. This approach enables us to remove the metal contribution in the forest *directly* and to recover one long continuous metal-free forest spectrum, and also to obtain an improved estimate of the continuum level.

The paper is organised as follows. In Section 2, we describe the data used for our analysis. In Section 3, we present the Voigt profile fitting analysis used to remove the metal contribution in the forest. We investigate systematics of uncertainties affecting the flux PDF in Section 4. The observed flux PDF function and effective optical depth are presented in Section 5. Our conclusions are given in Section 6.

2 THE DATA

2.1 Description of the sample

We have selected a sample of 18 spectra from the LUQAS sample (Kim et al. 2004) of 27 spectra obtained with VLT/UVES (Dekker et al. 2000). The spectra in LUQAS (Large sample of UVES QSO Absorption Spectra) were taken from the ESO archive and a large fraction of them were observed as part of the Large Program 166.A-0106 (Bergeron et al. 2004). The observations were performed in the period 1999–2004. All spectra have high signal-to-noise ($S/N \geq 25\text{--}30$) in the Ly α forest region and a resolution of $R \sim 45\,000$. The wavelengths are helio-centric and vacuum-corrected. The spectra were sampled with pixels of width 0.05 \AA .

From the 27 spectra in the LUQAS sample, we have chosen those with a S/N in the forest region of at least 30–50,

a full coverage of the Ly α forest and at least some coverage of the Ly β forest. Most of the 18 spectra cover the wavelength range of the higher order Lyman forest down to the atmospheric cut-off at 3050 Å. Some, however, cover only a part of the Ly β forest due to their low emission redshift. For Ly α absorption at $z \leq 1.99$ the corresponding Ly β absorption is not covered in these optical spectra. Note that we did not include the spectrum of HE1341–1020 which would have met these criteria but is a mini-BAL.

In Table 1 we list the characteristic properties of the 18 QSO spectra in our sample. The signal-to-noise ratio is per pixel with the first (second) number corresponding to the lower (upper) limit of the wavelength range analysed. Note that the S/N is not constant across the spectrum. To avoid the proximity effect, we excluded a region corresponding to 4,000 km s⁻¹ bluewards of the Ly α emission line. Lyman limit absorption systems (LLSs) with column densities $10^{17.2} \text{ cm}^{-2} \leq N_{\text{H I}} < 10^{19} \text{ cm}^{-2}$ are included in our flux distribution study, while 50 Å segments of the spectra have been excised to the left and right of the centre of sub-damped Ly α absorption systems (sub-DLAs, $N_{\text{H I}} = 10^{19-21.3} \text{ cm}^{-2}$). None of our spectra contain a damped Ly α system ($N_{\text{H I}} \geq 10^{21.3} \text{ cm}^{-2}$) in the observed wavelength range down to either the atmospheric cutoff or at the Lyman limit discontinuity caused by LLSs or sub-DLAs along the spectra with non-zero observed fluxes.

The Ly α forest regions of the spectra were grouped into 3 redshift bins with median redshifts $\langle z \rangle = 2.07, 2.52$ and 2.94 , as shown in Fig. 1 and listed in Table A1 in Appendix A. We have chosen these redshift bins as a compromise between minimising the Poisson fluctuations of the statistical quantities we are interested in and being able to investigate their redshift evolution. As we will show in section 5.1, spatial fluctuations in the flux PDF are large and substantial redshift paths are necessary to reduce the the Poisson *noise* from individual absorption systems. If an object contains an absorption profile which straddles a redshift bin boundary we have assigned it to the redshift bin in which most of it lies, and adjusted the wavelength range contributed by that QSO accordingly.

The spectra used here are essentially the same as those used in Kim et al. (2004) in the analysis of the LUQAS sample. There are, however, three differences between the spectra in the LUQAS sample and the spectra analysed here:

First, additional data for HE1122–1648, HE2347–4342 and PKS2126–158 has been obtained since the LUQAS data reduction. The additional data has been reduced with MIDAS/UVES as described in Kim et al. (2004), and added using the UVES_popler (UVES POst PipeLine Echelle Reduction) program¹, resulting in significantly larger S/N for the spectra of these three QSOs.

Second, we have re-reduced and performed a first-order flux calibration for the spectra of four QSOs (Q0420–388, HE0940–1050, Q0002–422 and HE2217–2818) in order to estimate the normalisation uncertainty between calibrated spectra and un-calibrated spectra. The UVES spectra do not normally have an absolute flux calibration, due to the lack of well-calibrated standard stars with spectra taken at the

resolution of the instrument². Consequently, most spectra in the LUQAS sample were not flux-calibrated. Even in the few cases where flux calibrations were performed, such as for HE2217–2818, these were done echelle order by echelle order and are far from perfect. It is not uncommon for a standard star to have strong hydrogen Balmer series with a width larger than a echelle order (~ 25 Å), and then the spectrum cannot be properly flux-calibrated in this way. A lack of a proper flux calibration and deficiencies in the flat-fielding procedure sometimes leave unwanted, oscillatory features in the extracted spectrum, with periods corresponding to the scale of one echelle order. The flux is then higher at the central wavelength and lower at both ends of a given echelle order compared to the flux at the same wavelengths from adjacent echelle orders. In addition, the non-calibrated spectra show a different continuum shape for the same wavelength regions covered by the different CCDs. These deficiencies aggravate the difficulties of continuum fitting the spectra, especially at high redshifts. Instead of an order-by-order flux calibration, we performed a first-order flux calibration as follows. We corrected each merged science spectrum using the master response function³ provided by ESO for a given observing period. When the master response functions were not available for a particular period, we scaled the un-calibrated spectra to the flux-calibrated spectra from other periods. The flux-calibrated spectra were then combined as described in Kim et al. (2004).

Third, and most importantly, we performed new continuum fits to all spectra in the sample optimised for a Voigt profile analysis. The normalised LUQAS spectra and the normalised spectra analysed here therefore differ slightly. Details of the continuum fitting are described in the next section.

2.2 Continuum fitting

The absorption due to intervening neutral hydrogen and metals is imprinted on the QSO emission spectrum, which has several, normally broad, emission lines overlaid on continuum emission from thermal and non-thermal radiation processes. The spectral energy distribution (SED) of the emission therefore varies significantly between different QSOs.

Most statistical analysis of the absorption thus require the fitting of a *continuum* characterising the SED of the unabsorbed emission of the QSO (see Lidz et al. (2006) for a recent study that uses spectra that are not normalised in this way). Careful continuum fitting is particularly important for a Voigt profile analysis of QSO absorption spectra such as the one performed here. Estimating the unabsorbed emission is particularly difficult at high redshifts where an increasing fraction of the spectrum shows significant absorption. The problem of continuum fitting has been extensively discussed in the literature (Kim et al. 2002; Bernardi et al.

¹ http://astronomy.swin.edu.au/mmurphy/UVES_popler.html, kindly provided by Dr. M. Murphy.

² The UVES pipeline reduction program determines the large-scale continuum shape from the ratio of the spectral shape of the target and the flat-field flux. For a fixed instrumental setting, the extracted spectra of the same object show a more or less similar shape of the large-scale continuum.

³ http://www.eso.org/observing/dfo/quality/UVES/qc/std_qc1.html

Table 1. Analysed QSOs

QSO	z_{em}^{a}	$z_{\text{Ly}\alpha}$	$\lambda_{\text{Ly}\alpha}(\text{\AA})$	S/N	Continuum (%) ^b	Lyman limit ^c	notes ^d
Q0055–269	3.655 ^e	2.936–3.205	4785–5112	80–50	1–3	2288	
PKS2126–158	3.279	2.815–3.205	4638–5112	50–200	1	3457	two sub-DLAs at $z = 2.768$ & 2.638
Q0420–388	3.116 ^e	2.480–3.038	4231–4909	100–140	1	3754	a sub-DLA at $z = 3.087$
HE0940–1050	3.078	2.452–3.006	4197–4870	50–130	1–2	≤ 3200	
HE2347–4342 ^f	2.874 ^e	2.336–2.819	4055–4643	100–160	1–2	...	multiple associated systems
Q0002–422	2.767	2.209–2.705	3901–4504	60–70	2	3025	
PKS0329–255	2.704 ^e	2.138–2.651	3815–4439	30–55	2–4	3157	associated system at 4513.7 \AA
Q0453–423	2.658 ^e	2.359–2.588	4084–4362	90–100	1–2	3022	a sub-DLA at $z = 2.305$
		2.091–2.217	3758–3911	60–100	1–2		only for the H I opacity
HE1347–2457	2.609 ^e	2.048–2.553	3705–4319	85–100	2	2237	
Q0329–385	2.434	1.902–2.377	3528–4105	50–55	2–3	≤ 3050	
HE2217–2818	2.413	1.886–2.365	3509–4091	65–120	1–2	2471	
Q0109–3518	2.405	1.905–2.348	3532–4070	60–80	2	2163	
HE1122–1648	2.404	1.891–2.358	3514–4082	70–170	1–2	≤ 1629	
J2233–606	2.250	1.756–2.197	3335–3886	30–50	2–4	≤ 1750	
PKS0237–23	2.223 ^e	1.765–2.179	3361–3865	75–110	1–2	≤ 3050	a sub-DLA at $z = 1.673$
PKS1448–232	2.219	1.719–2.175	3306–3860	30–90	2–4	≤ 3050	
Q0122–380	2.193	1.700–2.141	3282–3819	30–80	2–4	≤ 3052	
Q1101–264	2.141	1.880–2.097	3503–3765	80–110	1–2	2597	a sub-DLA at $z = 1.839$
		1.659–1.795	3233–3398	45–75	2–3		only for the H I opacity

^a The redshift is measured from the observed Ly α emission line of the QSOs. The redshift based on the emission lines is known to be under-estimated compared to the one measured from the absorption lines of the host galaxies (Tytler & Fan 1992; Vanden Berk et al. 2001).

^b Rough estimate of the continuum fitting uncertainty. It varies across the spectrum.

^c The wavelength of the Lyman limit for each spectrum is defined here as the wavelength below which the observed flux is zero. This does not necessarily correspond to the Lyman limit of an identified Lyman limit system/sub-damped Ly α system. Whenever a FOS/HST or STIS/HST spectrum is not available, the Lyman limit is assumed to occur at the shortest observed optical wavelength. FOS/STIS spectra from the HST archive are available for the following QSOs (any snap-shot survey or spectra with very low S/N are not used): Q0055–269: FOS (PI: Burbidge, Proposal ID: 3199); HE2347–4342: STIS (PI: Heap, Proposal ID: 7575; PI: Kriss, Proposal ID: 8875), FOS (PI: Reimers, Proposal ID: 6449), GHRS (PI: Reimers, Proposal ID: 6449); Q0002–422: FOS (PI: Rao, Proposal ID: 6577); Q0453–423: FOS (PI: Rao, Proposal ID: 6577); HE1347–2457: STIS (PI: Webb, Proposal ID: 9187); HE2217–2818: STIS (PI: Webb, Proposal ID: 9187); Q0109–3518: STIS (PI: Webb, Proposal ID: 9187); HE1122–1648: STIS (PI: Baldwin, Proposal ID: 9885), FOS (PI: Reimers, Proposal ID: 5950); J2233–606: STIS (PI: Williams, Proposal ID: 8058); Q1101–264: FOS (PI: Bahcall, Proposal ID: 5664)

^d In spectra with a sub-damped Ly α system, we discard at least 50 \AA on each side of the centre of the sub-DLA system.

^e The emission redshift is uncertain due to absorption systems at the peak of the Ly α emission line or the occurrence of multiple peaks.

^f The spectrum shows very strong O VI absorption blended with two saturated Ly α absorption systems at 4012–4052 \AA (Fechner et al. 2004). Since the line parameters for these Ly α systems cannot be well constrained (their corresponding Ly β is below the partial Lyman limit produced by the $z \sim 2.738$ systems), we discarded this wavelength region.

2003; Seljak et al. 2003; Songaila 2004; Tytler et al. 2004; Kirkman et al. 2005; Lidz et al. 2006) and we only summarise a few important points here.

First it should be noted that there are fundamental differences in the way continuum fitting is performed for low/intermediate resolution, low S/N data such as the SDSS Ly α forest data and high resolution, high S/N data obtained with high resolution spectrographs such as VLT/UVES and Keck/HIRES. For low/intermediate resolution, low S/N data the unabsorbed continuum level is normally estimated using a simple extrapolation from the much less absorbed region of the spectrum redward of the Ly α emission line at wavelengths $\lambda_{\text{rest-frame}} \geq 1250 \text{ \AA}$. The continuum is thereby assumed to be a power law with some superimposed emission lines (Press et al. 1993; Bernardi et al. 2003).

For high resolution, high S/N spectra the continuum is normally fitted by *locally* connecting apparently absorption-free regions (McDonald et al. 2000; Kim et al. 2004; Kirkman et al. 2005). This detailed local fitting of

a continuum is time consuming and ceases to work well once the redshift of the QSO becomes large ($z_{\text{em}} > 4$), where severe blending makes it impossible to identify any un-absorbed regions. In the redshift range considered here, $1.5 < z_{\text{em}} < 3.5$, however, this method still works well. We used it to determine an initial guess for the continuum level for the 18 spectra in our sample. Due to the high resolution, high S/N of our data, emission lines both weak and strong (mainly near 1073 \AA and 1123 \AA in rest-frame; Bernardi et al. 2003; Tytler et al. 2004) are easily identified in the forest, despite the lack of an appropriate flux calibration. The strong, broad ozone absorption bands at $\leq 3400 \text{ \AA}$ only affect the Ly α forest at the lower end of the redshift range of our sample (Schachter 1991). However, this is compensated for by the rather low density of absorption features at low redshift which leaves more absorption-free regions to fit the continuum in our high resolution, high S/N spectra.

Most of the spectra were not flux-calibrated, and the flat-fielding procedure was not always ideal, and as a conse-

quence there were some spurious broad features in a number of the spectra. Rather than attempt to fit the entire spectrum using an impractically high order function, the spectrum was divided into chunks. The size of these was determined interactively, and depended on the redshift and the presence of strong absorption systems. Typically these chunks were 150–300 Å long in the Ly α forest part of each spectrum, and at longer wavelengths ranged from ~ 200 Å in QSO emission lines up to ~ 1000 Å elsewhere. Legendre polynomials of order ~ 20 in the Ly α forest, and up to ~ 200 at longer wavelengths, were fitted to each chunk, using the IRAF CONTINUUM/ECHELLE procedure. These local continua were then combined to produce a single continuum for the entire spectrum, and any small discontinuities at the boundaries were adjusted manually to produce a smooth result. We will call the continuum obtained in this way the *initial* continuum, C_i .

As we will describe in the next section we have performed a full joined Voigt profile analysis of the H I and metal absorption in the spectra in order to obtain absorption line parameters (the redshift z , the column density N in cm^{-2} and the Doppler parameter or b parameter in km s^{-1}). The Voigt profile analysis is sensitive to the assumed continuum and the simultaneous fitting of different transitions caused by the same ion often reveals where the continuum should lie in absorbed regions of the spectrum. We have therefore adjusted our initial continuum C_i when we fitted absorption features with the Voigt profile fitting routine VPFIT⁴. The fitting procedure and the adjustment of the continuum level are very similar to the one described in Carswell, Schaye & Kim (2002) and will be discussed in more detail in Kim et al. (2007, in preparation).

For each spectrum, we first searched for metal absorption using the entire range of the available spectrum. The identified metal lines were the first to be fitted. During this process, the continuum was adjusted to obtain acceptable ion ratios. If the metal lines were blended with H I absorption features, the H I and metal lines were fitted simultaneously. Once all identified metal absorption was fitted we then fitted the rest of the absorption features assuming they are due to H I absorption. For this we used higher-order Lyman series lines whenever they were available to constrain saturated lines. In doing so, we further adjusted the continuum level to achieve a satisfactory fit for the available Lyman series. Using this *second* continuum estimated from the *first* profile fitting procedure, the profile fitting was repeated and the second continuum was checked manually again. This procedure was repeated several times, until we were satisfied with the results. The fitting was performed both by R. F. Carswell and T.-S. Kim independently, and the final fitting was carried out by T.-S. Kim. Note that we did not account for the possibility of an extended smoothly varying component of weak absorption often referred to as Gunn-Peterson absorption. We further assumed that the response function of UVES is smoothly varying for the non-calibrated spectra as seen in a smoothly varying master response function provided by ESO.

The *final* adjusted continuum obtained from the fitting procedure was then used to obtain the final normalised spec-

tra used in this study. When we use the term “continuum” in the following, it always refers to this *final* continuum, C_f . The difference between C_f and C_i is small and usually restricted to some limited wavelength regions, except in the regions around Lyman limit systems and sub-damped Ly α systems where the difference becomes rather large. We stress once again that these final continua are *different* from the continua used in Kim et al. (2004) which were estimated using the C_i procedure only. Note also that these final continua are not necessarily always completely smooth since in some regions of the spectrum continuum adjustments have been applied using a straight line to get reasonable column density ratios for different transitions. These small adjustments are required mainly because of the characteristics of the un-calibrated spectra, especially at shorter wavelengths at ≤ 3400 Å. The number of adjustments depends on the QSO and varies from none to several. Using a comparison between calibrated and non-calibrated spectra, we were able to correct some non-smooth features caused by instrumental artifacts.

Kirkman et al. (2005) have performed a very detailed study of the localised continuum fitting procedure used here using 24 high resolution, high S/N Keck/HIRES spectra. They tested their continuum fitting uncertainties using real and artificial spectra fitted by 4 different people. Kirkman et al. (2005) found noticeable differences between the fits by different people. Similarly, R. F. Carswell and T.-S. Kim did not agree on some parts of continuum fits of the spectra, confirming that such a continuum fitting procedure is not fully objective. However, given the complexity of the problem we cannot see a better way of doing it. We will later quantify the effect of continuum uncertainties on the flux probability distribution function and the effective optical depth due to H I absorption in Section 4 and 5.

The continuum uncertainty depends strongly on the S/N of the spectrum as listed in Table 1. The higher the S/N is, the smaller the continuum uncertainty is. In the upper panel of Fig. 2 we show the calibrated spectrum of Q0420–388, one of our best spectra with a S/N = 100–140. The lower panel shows the non-calibrated spectrum of PKS0329–255, one of the two worst quality spectra in our sample. For illustrative purpose we show the effect of a 5% decrease (C_{-5}) and increase (C_5) of the continuum level by the dashed curves. It is obvious that C_5 and C_{-5} dramatically over/under-estimate the continuum level in the case of Q0420–388. Even for PKS0329–255, C_5 and C_{-5} over/under-estimate the continuum in most parts. Unfortunately, a rigorous quantitative assessment of the continuum uncertainty is not possible given the complex nature of the continuum fitting process.

In Table 1 we give rough estimates of the continuum uncertainty obtained from absorption-free regions of the spectra. For this we compared the highest and the lowest flux levels in absorption-free regions to the average flux level in the same regions, disregarding localised excursions in only one pixel. Note that the continuum uncertainty is not constant across the spectrum. Note further that due to the possible presence of extended featureless absorption, the Gunn-Peterson absorption, the continuum used in this study is more likely to be an underestimate than an overestimate of the true continuum.

The two lowest quality spectra in the sample are

⁴ Carswell et al.: <http://www.ast.cam.ac.uk/~rfc/vpfit.html>

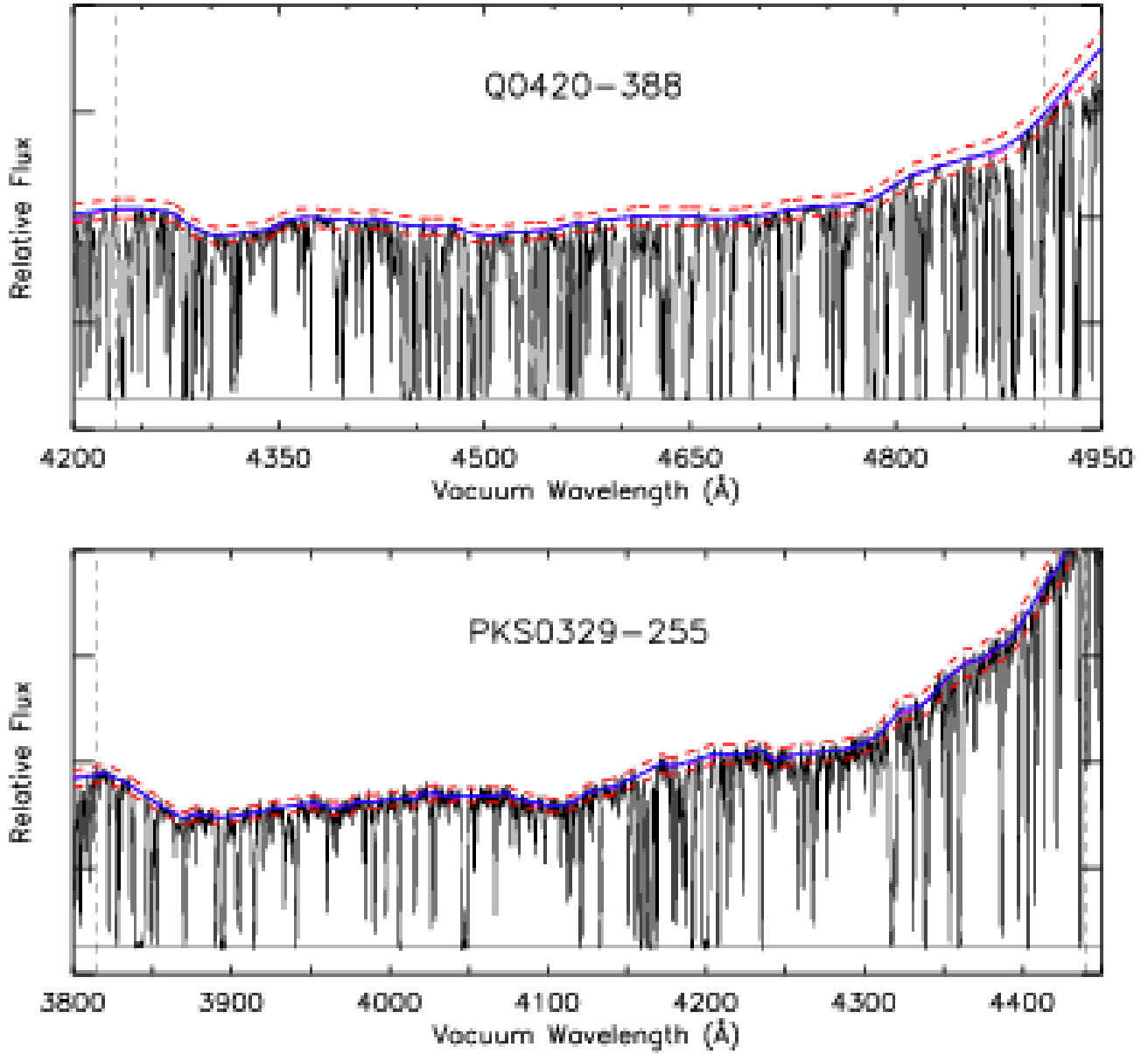


Figure 2. One of the best (Q0420-388 with $z_{\text{em}} = 3.166$, upper panel) and one of the worst (PKS0329-255 with $z_{\text{em}} = 2.704$, lower panel) quality spectra in our sample. The solid curves show our final continuum fit, while the dashed curves show a continuum level increased/decreased by 5%. The dot-dash curves which are almost indistinguishable from the solid curves are the initial continuum fit, C_i . The metal absorption has not been removed in both spectra. The spectrum of Q0420-388 is flux-calibrated and has one of the highest signal-to-noise ratios. We estimate the uncertainty of its continuum fit to be less than 1%. The spectrum of PKS0329-255 is not flux-calibrated and has low signal-to-noise ($S/N \sim 30-40$) in most parts of the spectrum. It also shows the largest residuals from the fitted line profiles and the largest zero flux offset. We estimate the continuum uncertainty to be 3-4% in the lower signal-to-noise regions. The vertical thin-dashed lines indicate the minimum and maximum wavelengths used in the analysis.

PKS0329-255 (lower panel of Fig. 2) and J2233-606. At 3700 Å, J2233-606 has a S/N of 30-35, and for PKS0329-255 the S/N is generally $\sim 30-40$. The continuum uncertainties are $\sim 3-4\%$ for the lower S/N regions and $\sim 2-3\%$ elsewhere. PKS0329-255 also has the largest zero flux-level offset (see the next subsection) in our sample. PKS1448-232 and Q0122-380 also have continuum uncertainties of $\sim 3-4\%$ in regions where the S/N is $\sim 30-35$, at

≤ 3550 Å and at ≤ 3450 Å, respectively. Fortunately most of our spectra have higher S/N , and the continuum uncertainties are generally around 1-2%.

2.3 Uncertainty of the zero flux level

As discussed in Kim et al. (2004), the UVES standard pipeline reduction program returns spectra where the sky

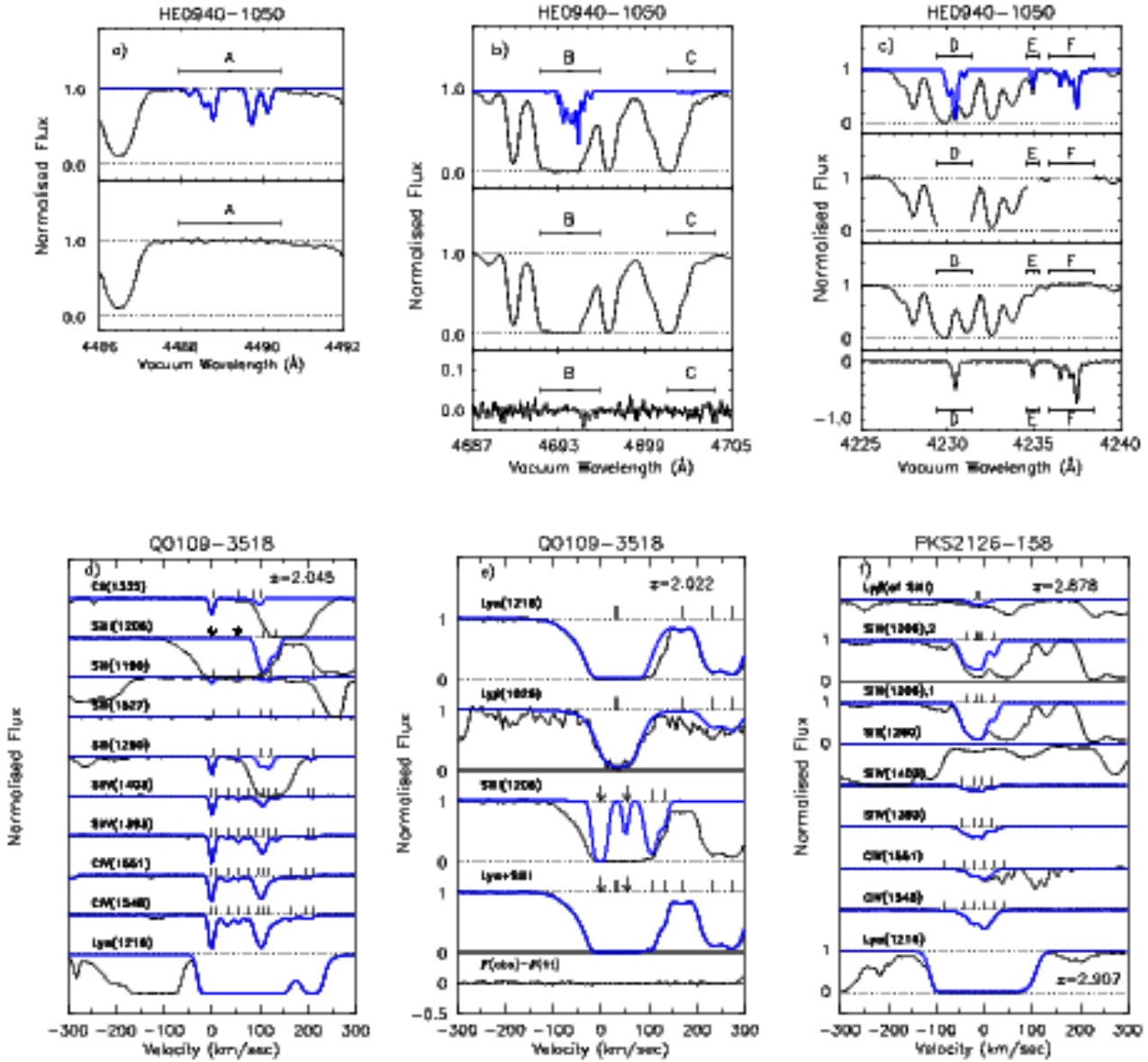


Figure 3. Various examples of metal absorption in the Ly α forest region of the spectra in our sample. Thin and thick curves represent observed spectra and fitted line profiles, respectively. **a)** Region A in the upper panel shows an isolated metal absorption system, Si IV 1393 at $z = 2.221$ towards HE0940–1050. Fe II 1608 at $z = 1.789$ at 4485.4–4487.2 Å is not shown in order to make the figure simpler. The lower panel shows the spectrum after subtracting the metal absorption in region A and adding noise from nearby absorption-free regions. **b)** The thick solid curve in the top panel shows Fe II 1608 at $z = 1.919$ (region B) and Fe II 1611 at $z = 1.919$ (region C) in the spectrum of HE0940–1050. The line parameters for both absorption systems have been obtained from other less strongly blended Fe II transitions at other wavelengths. The fitted H I-only profile is shown in the middle and the difference between the observed profile and the fitted H I profile is shown in the bottom panel. **c)** Regions D, E and F in the top panel mark absorption by C IV 1548 at $z = 1.732$, C IV 1548 at $z = 1.735$ and a mixture of C II 1334 at $z = 2.175$ and C IV 1550 at $z = 1.732$ in the spectrum of HE0940–1050. The second panel shows the regions of this part of the spectrum not contaminated by metals. The fitted H I-only profile and the difference between the fitted H I-only and the observed profile are shown in the third and fourth panel, respectively. **d)** The absorption profile of a metal absorption system at $z = 2.045$ in the spectrum of Q0109–3518. The wavelength scale in this and the next two panels has been transformed to a corresponding Doppler velocity. The profiles of the Si IV and Si II absorption suggest that two Si III 1206 components exist at 0 km s $^{-1}$ and ~ 54 km s $^{-1}$ (indicated by the arrows) which are blended with saturated H I absorption. **e)** The velocity profile for Si III 1206 in the same system as in **d)**. The top panel shows the Si III region at $z = 2.045$. The superimposed line is the H I Ly α profile at $z = 2.022$. The second panel is the H I Ly β profile at $z = 2.022$. The profile fit used both Ly α and Ly β simultaneously, assuming no Si III (at $z = 2.045$) contribution. The third panel shows the Si III absorption profile with the two components at 0 and ~ 54 km s $^{-1}$, assuming the same line strength ratio for these two components as estimated from the resolved Si II and Si III absorption. The fourth panel is the generated profile of the H I ($z = 2.022$, top panel) and Si III absorption ($z = 2.045$). The bottom panel is the difference between the observed and the generated H I + Si III profiles. **f)** The velocity profiles of a metal line system at $z = 2.907$ towards PKS2126–158. The second panel shows the Si III profile assuming the contribution from the superimposed H I at $z = 2.878$ which was estimated from the corresponding Ly β profile (top panel). The third panel shows the Si III profile assuming no contribution from H I. The weak, broad Si II 1260 absorption (the strongest Si II transition in the optical spectra) in the fourth panel is assumed to be a non-detection.

level is somewhat under-subtracted. This problem becomes more severe at shorter wavelengths (≤ 3400 Å). The under-subtraction of the sky level results in a non-zero flux level within the troughs of saturated lines. The offset from zero flux depends on signal-to-noise and wavelength. For increasing signal-to-noise and longer wavelengths the offset from zero becomes smaller. The worst case is PKS0329–255 with a typical offset, $\Delta F_{\text{zero}} = 0.015$ in a spectrum normalised to unit continuum. Note that this QSO also has one of the worst overall continuum uncertainty. Most spectra have an offset of much less than $\Delta F_{\text{zero}} = 0.01$. An offset from zero flux can lead to significant problems for the Voigt profile fitting. Since the flux in saturated regions does not go to zero, VPFIT normally adds many narrow components whose flux minima do not reach $F \sim 0$ instead of fitting the saturated profiles with fewer strong components, unless one specifically allows the zero level to vary. Fortunately, this problem has a negligible effect on the statistics of the flux distribution presented here, as will be discussed in more detail in Section 4.4.

3 A FULL VOIGT PROFILE ANALYSIS OF THE H I AND METAL ABSORPTION

Most simulations and models of the Ly α forest account only for the distribution of H I. In reality, the Ly α forest contains significant absorption from intervening metals in the IGM. These metal absorption lines are obviously interesting in their own right and provide a wealth of information on the spectrum of the metagalactic UV background and the metal enrichment of the IGM by galaxies. For a statistical analysis of the H I absorption aimed at studying the underlying matter distribution, they are, however, a source of contamination which leads to additional uncertainties. In this case it is therefore important to identify the metal lines in the forest and to remove them from further study, or at least to quantify their effect on any statistic investigated. Most studies so far have dealt with this problem by excluding spectral regions with strong metal contamination from the analysis, e.g. a strategy adopted by Rauch et al. (1997), McDonald et al. (2000) and Lidz et al. (2006).

The metal contamination is, however, rather widespread and varies strongly between different spectra. Excluding contaminated regions is therefore problematic. If metal lines are isolated, it is straightforward to excise the metal-contaminated regions. More often than not, metal absorption is, however, blended with H I absorption at $2 < z < 3.5$ ⁵. It is then difficult to decide which regions to exclude. Since there are only a few QSOs in each redshift bin in this

⁵ The amount of the metal absorption blended with H I absorption depends on redshift. At low redshift ($z < 2.5$) the H I absorption is weaker and most metal absorption occurs in region with weak or no H I absorption. At higher redshift ($z > 2.5$), the number density of H I absorption features increases and the metal absorption starts to blend in regularly with the H I absorption. At very high redshift ($z > 3.5$ –4), the density of H I absorption features becomes very high and many lines become saturated. In this case, many metal lines are blended with strongly saturated H I absorption and their contribution to the total absorption diminishes or becomes negligible.

and other similar studies, attempts to exclude metal contaminated region are likely to lead to a selection bias, especially at $z \sim 3$.

We take a different approach here, capitalising on a full Voigt-profile analysis of the H I and metal absorption performed by R. F. Carswell and T.-S. Kim which will be described in more detail elsewhere (Kim et al. 2007, in preparation). In this Voigt profile analysis we have identified all metal lines in the 18 spectra to the best of our knowledge. This allows us to remove their absorption contribution from the observed flux distribution. This method produces an estimate of the continuous flux distribution without any absorption due to *identified* metal lines.

For the identification of metal lines, we made use of known properties of metal absorption:

- (i) Metal absorption features tend to be narrower than H I lines.
- (ii) Metal absorption features are usually associated with strong, often saturated H I absorption.
- (iii) In the redshift range considered here, it is unlikely for H I absorption to show corresponding Si II without showing C IV, C II, Si IV or Si III. In short, H I absorption with no corresponding C IV is unlikely to show other metal lines, especially for the weaker absorption systems with column density $N_{\text{H I}} \leq 10^{14} \text{ cm}^{-2}$.

We started by identifying metal absorption features redward of the Ly α emission where all absorption lines (apart from the telluric lines, which were omitted) are due to metals. Most of these are C IV, Si IV, Si II, Al II, Al III, Mg II and Fe II. The rest-frame wavelengths and oscillator strengths for transitions from these ions are given by Morton (2003). Using these lines as a guide, we looked for other metal lines at the same redshift, such as C III, O VI, C I. In a second step we searched for metal lines associated with H I absorption with any column densities in the UVES spectra, i.e. at ≥ 3050 Å. Thirdly we looked for possible doublet candidates in the forest. In a fourth and final step we looked for possible metal lines associated with saturated H I absorption or with the Lyman discontinuity shown in the HST data listed in Table 1, i.e. at ≤ 3050 Å.

With information on absorption systems at $z < 1.5$ available for only half of the QSOs (see Table 1) and none of them observed at as high a resolution and S/N as the UVES data, it is very difficult to identify *all* the metal lines in the forest. Severe line blending often makes the identification of metal lines difficult. Sometimes an absorption feature first thought to be due to H I did not show a corresponding Ly β line of the expected strength when we attempted to fit higher-order Lyman series lines. Any excess absorption at the Ly α wavelength was then considered as being due to yet to be identified metal lines.

All other absorption not identified as being due to metals we have assumed to be due to H I. There were a few complexes of strong clustered rather narrow lines (Doppler parameters less than 15 km s^{-1}) which we suspect to be unidentified metal lines. We have flagged these as potential metal lines. These occasions, however, were rare. Note that some of the weak narrow lines which we considered as due to H I absorption could still be either weak, unidentified metal lines or noise peaks, while stronger metal lines are almost complete in their identification.

The different metal lines and H I were all fitted independently. Only the transitions produced by the *same ion* of the same redshift systems were required to have the same redshift and the Doppler parameters. Sometimes part of a given metal line is blended with strong H I absorption which makes it difficult to separate the metal and H I lines. *Only* in such circumstances, the redshifts and the Doppler parameters were *tied* with the ones measured from the other clean metal lines within the same ionisation group (such as Mg II, Fe II, C II and Si II for the low-ionisation group), similar to the method usually employed in the metal analysis of damped Ly α systems. Fortunately, most common metal lines embedded in the forest, such as Mg II, Fe II, Si II, C IV, are multiplets. Identifying these lines is more reliable than single-transition lines, such as Si III 1206.

While we are likely to have identified almost all strong metal lines, we would like to stress again that we will inevitably have ascribed some weak lines wrongly as being due to H I.

Fig. 3 shows some examples of the metal lines embedded in the forest. It also illustrates how we have subtracted the metal contributions from the flux distribution. Thin lines are the observed profiles (H I+metal lines), while the thick lines are the *fitted* H I or metal lines. The upper panel of Fig. 3 a) shows a single isolated metal system and the lower panel shows the same region after removing the metal lines and adding the noise estimated from nearby, absorption-free regions. About 40–50% of metals are isolated at $z \sim 2$, the fraction decreases to 20–30% at $z \sim 3$, due to increased Lyman line blending.

The top panel of Fig. 3 b) shows a moderate-strength metal line blended with H I absorption. Such embedded metal lines have been identified by other transitions falling outside the forest region or in regions of the forest where the H I absorption is weak. The middle panel shows the H I-only absorption profile generated from the parameters obtained from the line fitting. The lower panel shows the difference between the flux in the top (H I+metal) and middle panels. The difference is of the same order as the pixel noise. If metal absorption of weak to moderate strength is blended with saturated H I absorption, the metal absorption contributes very little to the combined absorption profile.

Fig. 3 c) shows a very common configuration of metal absorption. Approximately 45% of metal absorption systems at $z \sim 2$ and $\sim 75\%$ at $z \sim 3$ look similar to this. The top panel shows a region of a spectrum overlaid with the metal absorption profile of identified metal lines. In region D the metal absorption is blended with moderate-strength H I absorption. If we wanted to excise the metal absorption it is not obvious if one should cut out the entire H I absorption complex from 4226 Å to 4236 Å or only the region where the metals affect the H I profile from 4229.5 Å to 4231.2 Å as shown in the second panel. The third panel shows instead the H I-only absorption profile generated from the parameters obtained from our line fitting procedure. The bottom panel shows the difference between the H I and the H I+metal profiles.

The most difficult metal absorption features to obtain a reliable line fit for in the Ly α forest region of the spectrum is the absorption due to the single transition of Si III at 1206.5 Å (see McDonald et al. 2006). Sometimes we could successfully fit Si III absorption profiles blended with H I ab-

sorption using other metal lines, such as Ly α , Ly β , Si II, Si IV, Al III, Al II, C II, C IV, and Mg II. Sometimes, however, we could fit only part of a Si III profile. In such cases some contamination of the final H I profile is unavoidable, since we could not subtract all of the Si III contribution from the H I+Si III absorption feature. An example is shown in Fig. 3 d) and e).

Fig. 3 d) shows a typical metal line system at $z = 2.045$ towards Q0109–3518 where Si III is blended with H I absorption at $z = 2.022$. Note that we plot relative velocities here instead of wavelength as is customary for strong metal absorption complexes. The low (high) ionisation lines Si II (Si IV) suggest that there should be two components of Si III at 0 km s $^{-1}$ and ~ 54 km s $^{-1}$ in the saturated H I profile at $z = 2.022$, as indicated by the arrows. The top panel of Fig. 3 e) shows the Si III region of the system shown in panel d). Superimposed is the H I Ly α profile at $z = 2.022$, which was fitted together with the corresponding Ly β absorption (second panel), assuming no Si III (at $z = 2.045$) contribution. The third panel shows the Si III profile with the two components at $v = 0$ and ~ 54 km s $^{-1}$ (indicated by the arrows). These two components were generated assuming the same relative line strengths between all *successfully* fitted Si II and Si III components. In the 4th panel the H I Ly α (at $z = 2.022$) + Si III components (at $z = 2.045$) are superimposed. Note that the fit parameters of the H I profile are the same as in the first panel. The bottom panel shows the difference between the observed and the fitted H I Ly α + Si III profiles. The figure demonstrates that if the H I absorption is saturated, then even strong metal lines do *not* contribute significantly to the overall profile, unless the metal absorption extends to the wings of the saturated H I absorption profiles.

Fig. 3 f) shows a velocity plot of a metal line system at $z = 2.907$ towards PKS2126–158. It illustrates the uncertainty of the profile fit for a single transition Si III 1206 and a very weak line. The second and the third panels show the Si III 1206 absorption, assuming a H I contribution at $z = 2.878$ constrained by the corresponding Ly β (the top panel indicated by a thick tick mark) and assuming no H I contribution, respectively. In reality, its *true* column density could range between the ones obtained with these two assumptions. Similarly, the weak, broad feature at the expected location for Si II 1260 (the strongest Si II transition available in the spectra) in the fourth panel could be a real detection blended with weak H I (the upper limit for $N_{\text{Si II}}$ can be estimated from non-detection of other Si II transitions above the Ly α emission) or a weak broad H I. Since we do not want to over-identify metals and want to be *conservative*, we adopted the lowest Si III 1206 column density (assuming a contribution by H I) and considered Si II 1260 to be not detected in this case. Only when it was not possible to constrain H I from higher order Lyman series, we assumed that the absorption was due to metals only. Non-detection in Ly β in our spectra typically corresponds to $N_{\text{H I}} \leq 10^{12.8}$ cm $^{-2}$ assuming $b = 20$ km s $^{-1}$ (or $F \geq 0.8$ in Ly α). Fortunately there are not many such cases in our sample. In Table A2 in Appendix A we list uncertain line fits.

In summary, for each QSO we have obtained a Ly α forest spectrum free of identified metal lines as follows:

- for isolated metal lines the spectrum was replaced by

continuum with a noise level estimated from nearby continuum regions;

- where metal lines and H I lines are blended, that part of the spectrum was replaced with the model H I lines determined from fitting Voigt profiles to the heavy element and Lyman lines simultaneously, with noise using estimates appropriate to the final flux levels determined from nearby regions.

In Fig. 4 we show the continuum fitted spectra of our complete sample together with the metal contribution to the total absorption to give a general impression of the metal contamination. Note that the metal contribution to the total absorption differs significantly from the metal-only absorption as metal absorption blended with strong H I has little effect on the total absorption profile.

4 STATISTICAL ERRORS AND SYSTEMATIC UNCERTAINTIES OF THE FLUX PROBABILITY DISTRIBUTION

4.1 Statistical errors

One of the main aims of the paper is to estimate the H I-only absorption flux PDF from the normalised spectra of our sample. The PDF of the flux is simply the number of pixels which have a flux between F and $F + \Delta F$ for a given flux F divided by the total number of pixels (Jenkins & Ostriker 1991; Rauch et al. 1997; Bryan et al. 1999; McDonald et al. 2000; Kim et al. 2001).

Before presenting our new measurement of the flux PDF from our full sample we will discuss the statistical errors of the measured flux PDF and investigate some of the systematic uncertainties discussed in Section 2 on the flux. Following McDonald et al. (2000), we calculate the flux PDF for bins of width $\Delta F = 0.05$. Pixel with flux level smaller than $F = 0.025$ or greater than $F = 0.975$ have been allocated to the $F = 0$ bin and the $F = 1.0$ bin, respectively.

To estimate the errors of the PDF both for a single QSO and for a full sample, we used a modified jackknife method as presented by Lidz et al. (2006). We briefly outline the method here for clarity. We first calculate the flux PDF of the full sample. This sample was then divided into n_c chunks with a length of ~ 50 Å. If the PDF estimated from the full sample at the flux bin F_i is $\hat{P}(F_i)$ and the PDF estimated without the k -th chunk at the flux bin F_i is $\tilde{P}_k(F_i)$, then the covariance matrix $\text{cov}(i, j)$ between the PDF in a flux bin F_i and the PDF in a flux bin F_j was calculated as

$$\text{cov}(i, j) = \sum_{k=1}^{n_c} [\hat{P}(F_i) - \tilde{P}_k(F_i)][\hat{P}(F_j) - \tilde{P}_k(F_j)], \quad (1)$$

and the variance at a given flux level is given by the diagonal terms of the covariance matrix $\sigma_i^2 = \text{cov}(i, i)$ for a flux bin F_i . We checked that this modified jackknife method is not sensitive to the length/number of chunks for a given sample size. As expected, the errors are larger when the number of pixels in the sample is smaller: $\sim 15\%$ for Q0420–388 with 13561 pixels vs $\sim 7\%$ for the full $\langle z \rangle = 2.94$ sample with 34265 pixels at $F = 0.5$. We compared the errors obtained with the modified jackknife method with the errors obtained by 500 bootstrap realisations of chunks of 100 pixels (or 5 Å)

used by McDonald et al. (2000) and Schaye et al. (2003) (see Section 5.2 for more details for the bootstrap method). Both methods give comparable error estimates, while the Poisson errors (i.e. those based on the square root of the number of pixels) tend to be $\sim 35\%$ smaller.

4.2 Continuum fitting

We now move to a discussion of the effect of systematic uncertainties on the flux PDF. We start with the effect of continuum fitting uncertainties. In Fig. 5 we show the flux probability distribution of the spectrum of Q0420–388 including the metal absorption (see also Fig. 6) with our final continuum fit C_f , our initial continuum fit C_i and four further continua where we have applied a wavelength independent offset of the continuum level of $\pm 1\%$ (C_1 and C_{-1}) and $\pm 5\%$ (C_5 and C_{-5}). The dotted, dashed, solid, dot-dot-dot-dashed and dot-dashed curves show the PDF with C_5 , C_{-5} , C_f , C_1 and C_{-1} , respectively. The flux PDF of the spectra with the initial continuum fit C_i is almost indistinguishable from the PDF of the spectra with the final continuum fit C_f . As expected changing the continuum level affects the PDF most strongly at a flux level of $F \sim 1$, shifting the corresponding peak in the PDF. Continuum fitting uncertainties also have a moderate effect on the slope of the PDF at flux levels $0.65 < F < 1.0$. There is little effect at lower flux levels as regions of saturated or very strong absorption are not affected by an *over-/under-*estimated continuum as much as regions of weak absorption.

Note again that a systematic change of the continuum level by 5% is a gross overestimate of the actual continuum fitting uncertainty for most of our spectra. We choose this value here simply to demonstrate the effect more clearly. Most spectra in our sample have a continuum uncertainty of ~ 1 –2%, and the changes to the PDF are small.

4.3 Metal contamination

As apparent from Fig. 4 the metal contribution to the absorption varies significantly between different spectra. In Table A4 in Appendix A we quantify the metal contamination of the H I+metals effective optical depth, i.e. observed values before removal of the metal absorption, estimated using the effective optical depth after removal of the metal absorption. The values vary from 0.5% to 28% (note that in the case of Q0055–269, the metal removal is incomplete due to the limited wavelength coverage from 3200–6810 Å). There appears to be no obvious trend of the extent of the metal contamination with other parameters, such as z , except that spectra containing Lyman limit systems or sub-damped Ly α systems tend to show a larger absorption contribution by metals. The mean metal contamination is $\sim 12\%$. This is consistent within the errors quoted for *statistical* estimates of the metal contamination: $\sim 19\%$ at $z = 1.9$ by Tytler et al. (2004) and $\sim 10\%$ at $z = 2.7$ by Kirkman et al. (2005)⁶.

Fig. 6 illustrates the effect of absorption by metals on

⁶ Both removed the metals in the forest statistically. Using published line parameters *redwards* of the Ly α emission of QSOs at $1.7 < z_{\text{em}} < 3.54$, they estimated the amount of metals as a function of rest-frame and observed wavelength.

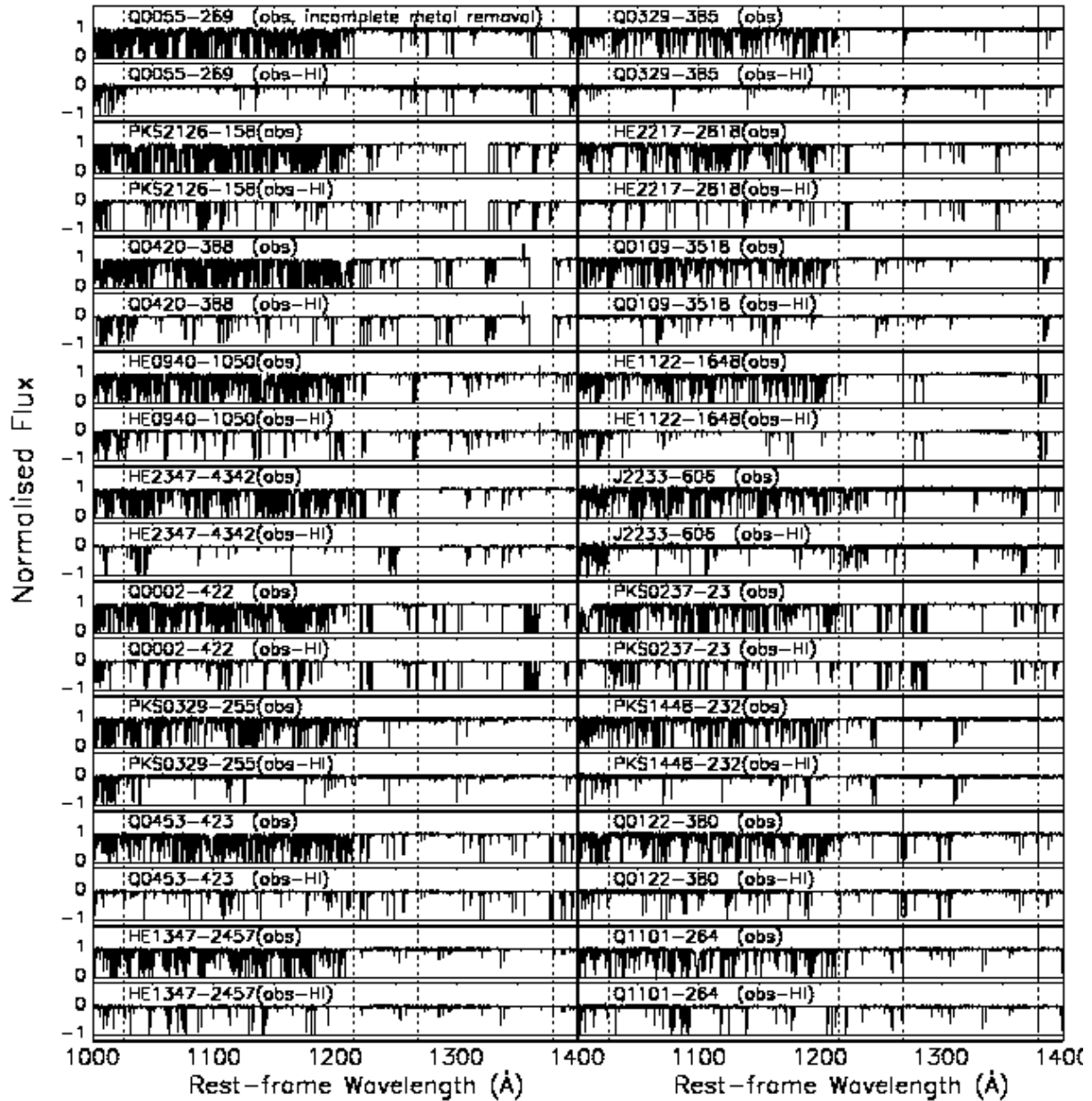


Figure 4. Normalised observed spectra and the additional metal contribution to the absorption for our sample of 18 VLT/UVES spectra (against rest-frame wavelength). The regions with no flux, such as at ~ 1315 Å of PKS2126–158, are due to the wavelength gaps caused by using three separate CCDs in the dichroic setting. The normalised observed spectra are shown by the thick solid curves in the upper panels for each QSO. Note that the lower panel is not the fitted metal absorption. It is the difference between the observed flux and the fitted H I absorption and thus shows the additional absorption by metals which is significantly smaller than the absorption by metals would be in the absence of H I absorption. The four vertical dotted lines indicate the rest-frame wavelength of Ly β , Ly α plus 1268 Å and 1380 Å. Note that the weak metal absorption at 1268–1380 Å does not necessarily indicate a low metal contamination in the forest (see e.g. the spectra of HE0940–1050 and HE1347–2457). The most common metal species found in high- z QSO spectra is C IV. The high column density absorption systems showing strong C IV (1548 Å and 1550 Å) and Si IV (1393 Å and 1402 Å) absorption features usually show other metal lines. These high column density absorption systems occur randomly along each sightline, i.e. at different z for different sightlines. Therefore, stronger transitions e.g. Fe II 2382 & 2600, Si II 1190, 1193 & 1260, or Mg II 2796 & 2803, which are usually associated with high column density systems, could be present in the Ly α forest region without there being any corresponding strong metal lines in the 1268–1380 Å range. The metal contribution in the spectrum of Q0055–269 forest could be significantly underestimated since the wavelength coverage in the red is rather limited, only up to 6809 Å (observed).

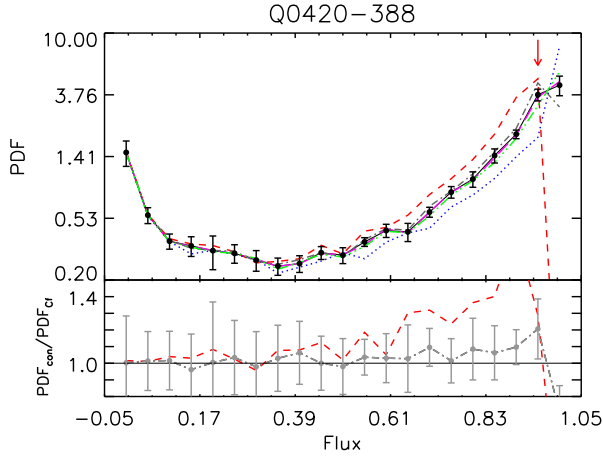


Figure 5. The upper panel shows the flux PDF of Q0420–388 ($2.480 < z < 3.038$) for 6 different continuum levels. The solid curve is the PDF for our best fit final continuum C_f , while the curve almost indistinguishable from the solid curve is the PDF for the initial continuum C_i . The dotted/dashed curve are the PDF for a continuum level increased/decreased by 5% (C_5 and C_{-5}), while the dot-dot-dot-dashed/dot-dashed curve are for a continuum level increased/decreased by 1% (C_1 and C_{-1}). The errors were estimated using a modified jackknife method by Lidz et al. (2006) as described in the text. Different continuum fits also shift the peak of the PDF, as indicated by the arrow for C_{-5} . The lower panel shows the following ratios $\text{PDF}_{C_5}/\text{PDF}_{C_f}$ (dashed curve) and $\text{PDF}_{C_{-1}}/\text{PDF}_{C_f}$ (dotted curve). The errors in the lower panel are similar for both curves but plotted only once for clarity. The errors correspond to the combined errors of both PDF_{C_5} and PDF_{C_f} .

the flux PDF. The upper panel shows the PDF of two artificial spectra which were generated from the fitted line parameters of PKS2126–158. The solid curve is the PDF after removal of the identified metal lines while the dotted curve is the PDF before removal of the metal absorption. The bottom panel shows the ratio of the two. Unlike continuum uncertainties metal absorption affects the flux PDF mostly at flux levels in the range $0 < F < 0.6$ even though there is also a small reduction of the flux PDF at $F \sim 1$. Note that the latter effect is likely to be underestimated as weak metal absorption is difficult to identify. Since the number of absorption features which we classified as *suspected* metal lines are small and usually weak, these lines have a negligible effect on the PDF at $0.1 < F < 0.6$.

4.4 Pixel noise and the uncertainty of the zero flux level

Pixel noise will cause a slight smoothing of the flux PDF. For high-S/N spectra as in our sample the effect is small but noticeable. This is demonstrated in Fig. 7. The upper panel shows the flux PDF of PKS0329–255 for the observed spectrum with metals (dot-dashed curve) and without metals (solid curve with error bars). The observed spectrum has $S/N = 30\text{--}55$. We generated 4 artificial spectra with different S/N using the fitted line parameters, assuming Gaussian noise: the dashed curve is for $S/N = 25$, the dotted curve is for $S/N = 50$, and the two almost indistinguishable thin

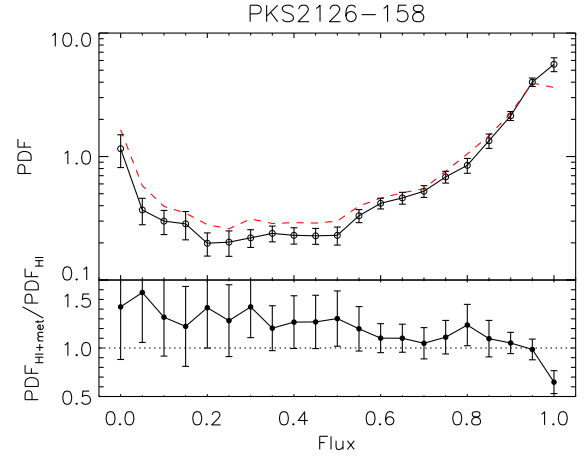


Figure 6. The upper panel shows the flux PDF of PKS2126–158 with metal absorption (dashed curve) and without metal absorption (solid curve). The two spectra were generated using fitted line parameters. The lower panel shows the ratio of the flux PDF with and without metals. The errors in the lower panel are the combined errors. The metal lines contribute to the flux PDF significantly at flux levels $F < 0.6$.

solid curves are for $S/N = 100$ and $S/N = \infty^7$. Note that the generated spectra do not have a offset from the zero flux level, i.e. the saturated lines go down to $F = 0$. The bottom panel shows the ratio of the PDF for the artificial spectrum with $S/N = \infty$ (solid curve) and the PDF for the spectrum with metals (dot-dashed curve) to the PDF of the metal-removed spectrum.

The effect of the signal-to-noise on the flux PDF is most evident at flux levels of $0 < F < 0.1$ as well as at $F > 0.9$, where it can exceed that from the metal contamination. At intermediate flux levels, $0.1 < F < 0.9$, the effect of the signal-to-noise is comparable or smaller than that due to metal absorption. It should, however, be noted here that the contribution of metal absorption in the spectrum of PKS0329–255 is rather small (2.8%) and that the spectrum has the lowest S/N of our sample.

In Fig. 8 we show the difference between the flux PDF of artificial $S/N = \infty$ spectra (i.e. no zero-level offset) and the flux PDF of the observed spectra without metal absorption for our full sample at three different redshift bins. At flux levels of $0.1 < F < 0.8$ the difference is less than 1% and much smaller than the statistical errors, but outside this range the errors increase to a few percent at low flux levels and more than 10% at high flux levels.

⁷ Note that the noise in the observed spectra is not exactly Gaussian. The noise at $F \sim 0$, i.e. the bottom of saturated lines, and at $F \sim 1$ are different, and of course the S/N at $F \sim 0$ is much worse than at $F \sim 1$. However, for the purpose of illustrating the S/N effect on the PDF, the assumption of Gaussian noise is a good approximation.

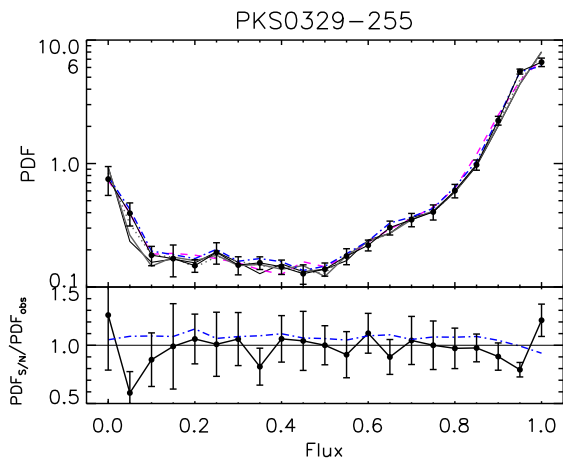


Figure 7. The upper panel shows the flux PDFs of the observed and artificial spectra of PKS0329-255 for different noise levels. The dot-dashed curve is for the observed spectrum including the metals, the solid curve with errors is for the observed spectrum after the metals have been removed. The four other curves are the flux PDFs for artificial spectra generated from the line parameters with different levels of Gaussian noise added. The dashed curve is for $S/N = 25$, the dotted curve is for $S/N = 50$ and the two almost indistinguishable thin solid curves are for $S/N = 100$ and $S/N = \infty$. The $S/N = \infty$ and $S/N = 100$ PDFs show a rather large deviation at $F < 0.1$ and almost a factor of 2 at $F = 0.05$. This is due to the offset of the zero flux level of the observed spectrum (a typical offset from zero flux is ~ 0.015) which the artificial spectra do not have and the effect of which is not smoothed out in the artificial spectra with the highest S/N . The lower panel compares the ratio of the flux PDFs of the $S/N = \infty$ spectrum to the metal-removed spectrum (solid curve) and the PDF ratio of the metal-included spectrum to the metal-removed spectrum (dash-dotted curve). The effect of low S/N on the flux PDF becomes noticeable at $F < 0.1$ and $F > 0.9$. At $0.1 < F < 0.9$, the effect of the S/N is comparable or smaller than that of the metal contamination.

5 THE FLUX DISTRIBUTION OF THE FULL SAMPLE

5.1 The flux probability distribution

Fig. 9 shows the main result of this paper, the flux PDF of the observed spectra in our full sample divided into three redshift bins (Table A1 in Appendix A) after removal of all identified metal lines. The thin, grey curves show the flux PDFs of the individual spectra. As found previously there is considerable scatter between different lines-of-sight. This is mainly due to the occurrence of strong absorption systems which are rare in individual spectra (Viel et al. 2004a). A considerable path length is therefore required to reach reasonable convergence to an average flux PDF. This is best illustrated by the spectrum of Q0002-422 which shows the most deviant individual PDF compared with the mean PDF in its redshift bin. This is probably due to several factors. The spectrum falls at the upper end of its redshift bin. It has also the shortest usable path length (191 Å) and the largest number of strong systems per unit redshift in the wavelength region used.

In Fig. 10 we show the effect of the removal of the identified metal absorption. The dashed and solid curves in the upper panel show the flux PDF of the spectra with

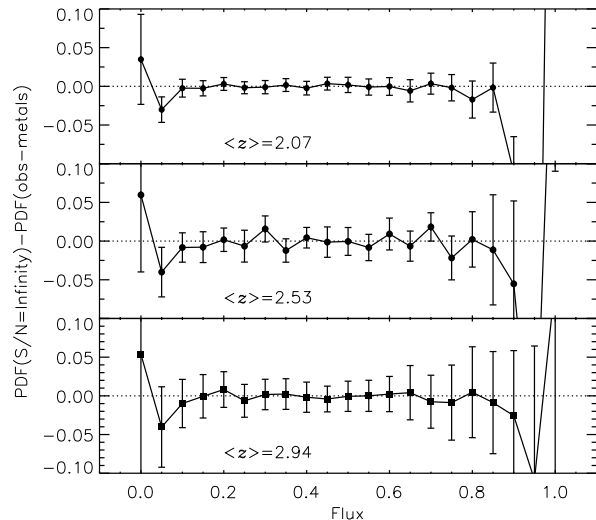


Figure 8. The difference between the flux PDFs for $S/N = \infty$ artificial spectra and metal-removed observed spectra for the full sample divided into three redshift bins. The errors are those of the PDF of the metal-removed observed spectra. The combined errors of both PDFs are larger. The effect of lower S/N and the offset of the zero flux level on the PDF are negligible compared to the statistical errors at flux levels $0.1 < F < 0.8$.

and without the identified metal absorption, respectively. The lower panel shows the ratio of the two. Removing the metal absorption mainly affects the flux PDF at flux levels $0.1 < F < 0.8$. Without metal absorption the fraction of pixels in this flux range is 10–20% lower. The effect of metal absorption, which appears to evolve little with redshift, is more significant at lower redshift where the H I absorption is smaller.

In Fig. 11 we compare our new measurement of the flux PDF with that of McDonald et al. (2000) at $\langle z \rangle = 2.41$ and $\langle z \rangle = 3.0$. The solid curves are the PDF when metals are included. Unfortunately a comparison at higher redshifts is not possible due to the lack of high-redshift spectra in our sample. At $\langle z \rangle = 2.41$ our measurement is about 10–20% lower at flux levels $0.1 < F < 0.5$ while at $\langle z \rangle = 3.0$ our measurement is about 10–30% lower at flux levels $0.2 < F < 0.8$. We can only speculate here where this discrepancy comes from. Part of the difference is probably due to the rather crude removal of metal absorption by McDonald et al., which is likely to have led to more residual absorption by unidentified metal lines in their spectra. The difference appears, however, to be larger than expected due to this effect and increases rather than decreases with increasing redshift. Note that the McDonald et al. sample is significantly smaller with a total of 8 spectra and some of the discrepancy can probably be explained as being due to variations between different lines-of-sight (see the grey thin curves in Fig. 9). Differences in the placement of the continuum level may also play a role. We list the mean flux PDF for the five different redshift bins discussed in this section in Table A3 in Appendix A.

The flux PDF is a statistical quantity which – at least in principle – can be easily compared with that of simulated spectra. Due to the expected tight correlation between H I

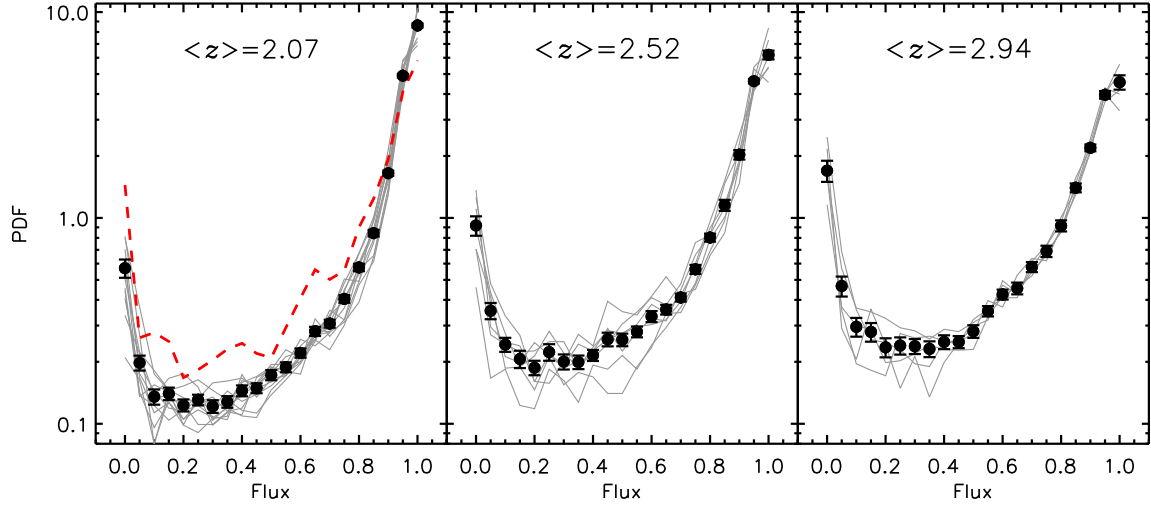


Figure 9. The flux PDF (filled circles with errors) of the full sample divided into three redshift bins after removal of the metal absorption. The thin grey curves show the PDFs of individual spectra. The 1σ error bars are estimated using a modified jackknife method (Lidz et al. 2006). The dashed curve in the $\langle z \rangle = 2.07$ bin is the PDF of the spectrum of Q0002-422, which has the highest redshift in this bin and the largest effective optical depth.

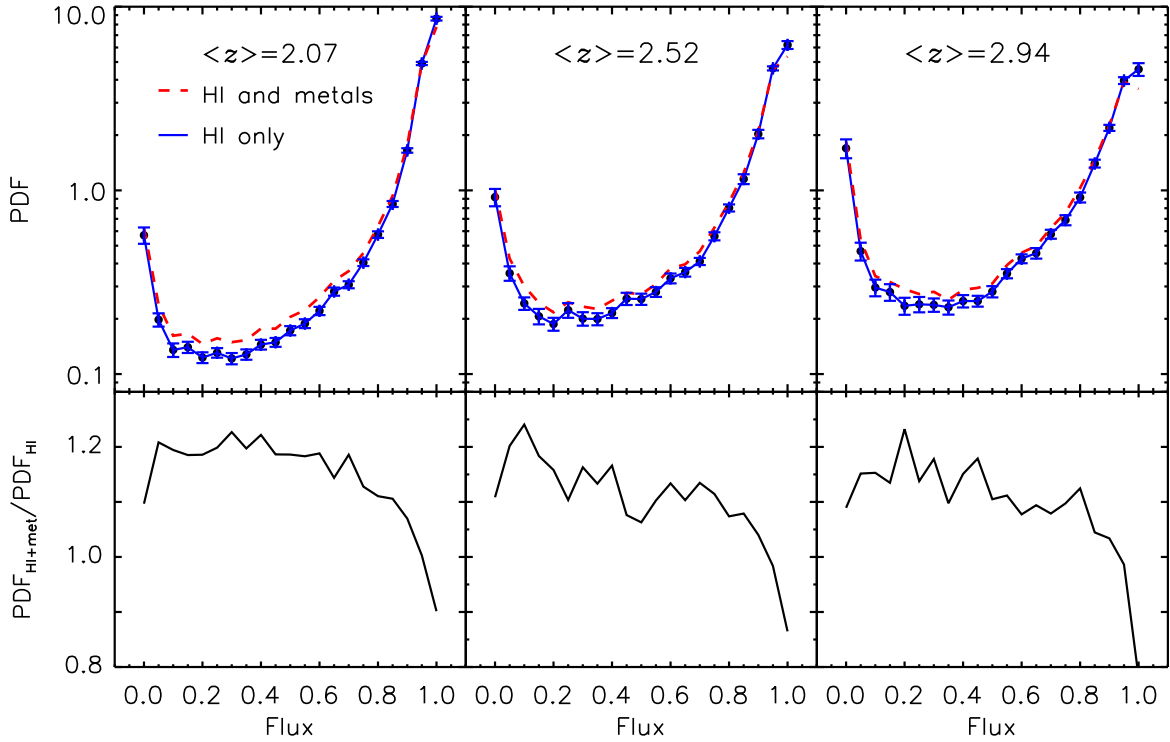


Figure 10. The flux PDF of the full sample divided into three redshift bins before (dashed curves) and after (solid curves) removal of the metal absorption. The lower panel shows the ratio of the PDFs before and after removal of the metal absorption. The effective optical depth due to H I absorption is lower at lower redshift and the relative contribution of the metal absorption is therefore larger.

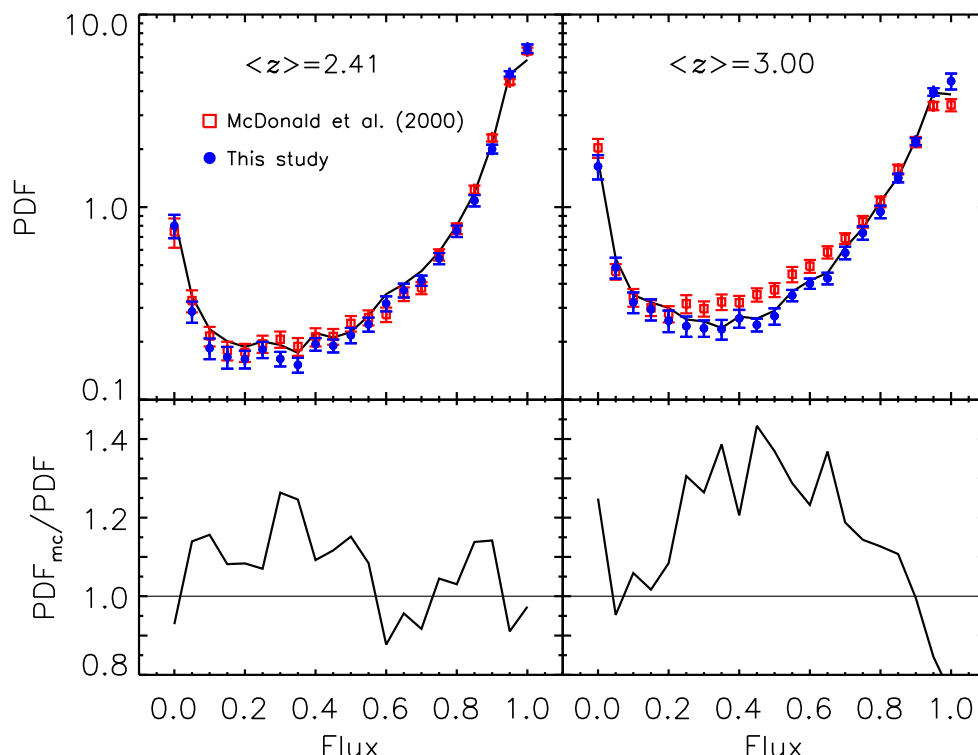


Figure 11. Comparison of the flux PDF of our sample divided into two redshift bins with that of McDonald et al. (2000). The solid curve and filled circles show the flux PDF of our sample before and after removal of the metal absorption, respectively. The lower panel shows the ratio of the flux PDF of McDonald et al. to that of our sample after removal of the metal absorption.

optical depth, local gas density and temperature, the observed flux PDF can constrain astrophysical parameters of the IGM as well as cosmological parameters (Weinberg et al. 1998; McDonald et al. 2000; Meiksin, Bryan & Machacek 2001; Desjacques & Nusser 2005). The effect of the removal of metal absorption and the difference to the published flux PDF by McDonald et al. is comparable or larger than the effect of changing some of the model parameters within plausible ranges (e.g. Meiksin et al. 2001; Desjacques & Nusser 2005). Our new improved measurement of the flux PDF should therefore be relevant for attempts to use the flux PDF to constrain astrophysical and cosmological parameters.

5.2 The H I effective optical depth

So far we have concentrated on the flux PDF of our sample. The H I effective optical depth ($\tau_{H I}^{\text{eff}}$) is another intensely studied quantity which is important for the comparison with models of the H I distribution. The H I effective optical depth is related to the mean flux as $\exp^{-\tau_{H I}^{\text{eff}}} = \langle \exp^{-\tau_{H I}} \rangle$, where $\langle \rangle$ indicates the mean value averaged over wavelength. Note that the effective optical depth is *not* the average of the optical depth. The effective optical depth is the quantity which directly goes into measurements of the amplitude of the metagalactic UV background (Rauch et al. 1997; Bolton et al. 2005) and plays a crucial role in calibrating

measurements of the matter power spectrum from Ly α forest data based on the flux power spectrum (Croft et al. 2002; Seljak et al. 2003; Tytler et al. 2004; Viel et al. 2004b; Lidz et al. 2006).

As we have taken special care with the removal of the metal absorption in our spectra it is worthwhile to revisit the effect the removal of the metal absorption has on the H I effective optical depth.

In Fig. 12 we show the effective optical depth of our observed spectra before (open squares) and after (filled circles) removal of the metal absorption. The solid lines in both panels is the power-law fit of $\tau_{H I}^{\text{eff}}$ to the optical depth of the high-resolution data from our sample and that compiled from the literature, $\tau_{H I}^{\text{eff}} = (0.0023 \pm 0.0007)(1+z)^{3.65 \pm 0.21}$ (the same power-law fit as in Fig. 13). The errors of $\tau_{H I}^{\text{eff}}$ were estimated with the same procedure adopted in McDonald et al. (2000) and Schaye et al. (2003)⁸. Each spectrum was divided into chunks of 100 pixels (or 5 Å). We then performed 500 bootstrap realisations, treating each chunk as a one data point. The removal of the metal absorption leads to a typical reduction in the *observed* effective optical depth (i.e. H I+metals) by 0.5% to 28% with the mean of $\sim 12\%$, albeit as expected

⁸ Note that the modified jackknife method using a ~ 50 Å-long chunk generally gives error estimates of only ~ 1 –2% for each QSO. These estimates are too low, since a $\pm 1\%$ continuum uncertainty generally gives an error of ~ 2 –10%.

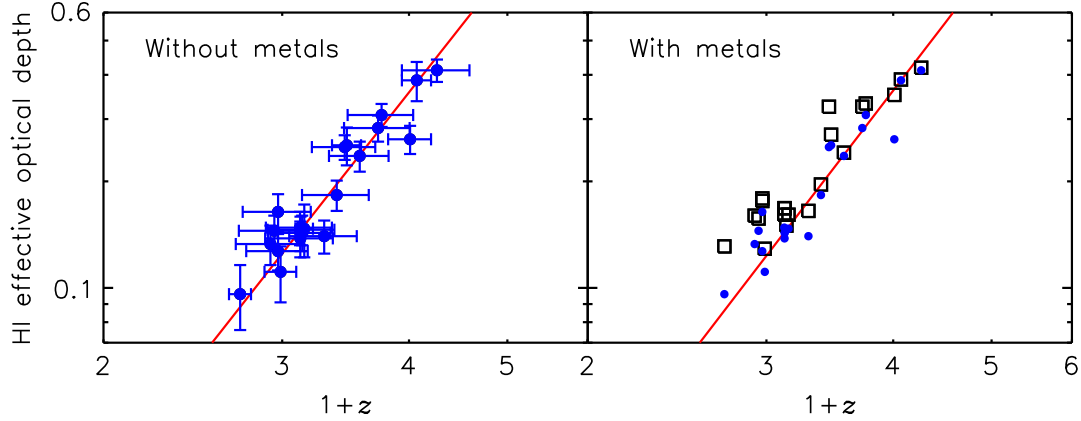


Figure 12. Left panel: Evolution of the effective optical depth of our full sample after removal of the metal absorption. The horizontal and vertical error bars show the redshift range used and the 1σ errors. The 1σ errors were estimated as in McDonald et al. (2000) and Schaye et al. (2003) using 500 bootstrap realisations of chunks of 100 pixels (5 Å). Right panel: Comparison of the evolution of the effective optical depth of our full sample before (open squares) and after (filled circles) removal of the metal absorption. The solid lines in both panels represent a power-law fit to the effective optical depth $\tau_{\text{H I}}^{\text{eff}}$ of our sample after removal of the metal absorption and other measurements from high-resolution data compiled from the literature at $1.7 < z < 4$ as in Fig. 13, $\tau_{\text{H I}}^{\text{eff}} = (0.0023 \pm 0.0007)(1+z)^{3.65 \pm 0.21}$.

with a large scatter (see Table A4 in Appendix A). As mentioned in Section 4.3, these numbers are estimated from the effective optical depths of the observed spectra before and after removal of the metal absorption. The H I effective optical depth is obviously also subject to the same systematic uncertainties as the flux probability distribution. The change of continuum from C_f to C_5 (C_1) increases $\tau_{\text{H I}}^{\text{eff}}$ by 0.049 (0.010), which is identical for each QSO. The noise and the uncertainty in the zero-level flux have a negligible effect on $\tau_{\text{H I}}^{\text{eff}}$.

The upper panel of Fig. 13 compares the $\tau_{\text{H I}}^{\text{eff}}$ measurements of our 18 QSOs with those of Schaye et al. (2003). Both set of values are measured from spectra where metal absorption has been removed. In the case of Schaye et al. (2003) this has been done by excising spectral regions contaminated with strong metal absorption. The values are in good agreement. Considering that half of the sample of spectra studied here is part of the sample of Schaye et al. (2003) this is not too surprising. For spectra common to both studies the differences are, in most cases, less than 10% when our wavelength ranges were adjusted to the ones used in the Schaye et al. sample⁹. Table A4 in Appendix A lists the measurement of $\tau_{\text{H I}}^{\text{eff}}$ as well as the mean flux, its variance and the contribution of metal absorption in the forest. The

errors are estimated from the 500 bootstrap realisations of a chunk of 5 Å.

In the lower panel of Fig. 13 we have compiled a range of $\tau_{\text{H I}}^{\text{eff}}$ measurements from the literature at $1.7 < z < 4$ and compare this with a measurement of $\tau_{\text{H I}}^{\text{eff}}$ from our sample after removal of the metal absorption binned in redshift bins with width $\Delta z = 0.2$ (filled circles with errors). Our $\tau_{\text{H I}}^{\text{eff}}$ is estimated from the mean flux of all pixels in each bin, instead of averaging the effective opacities of each QSO (see Table A5 in Appendix A). The errors are estimated by the 500 bootstrap realisations of 5 Å using all pixels in each bin. The open squares, filled squares and filled triangles show the measurements of Schaye et al. (2003), Kirkman et al. (2005) and McDonald et al. (2000), respectively. The filled diamond at $z = 1.86$ and the open circle at $z = 1.9$ are the measurements of Janknecht et al. (2006) and Tytler et al. (2004), respectively. Note that our values are in good agreement with those measured by Kirkman et al. (2005) at $1.7 < z < 3.3$, although the latter did not include any LLSs and removed the metal contribution statistically.

The solid line in Fig. 13 is the best power-law fit to the optical depth values of high-resolution data in the redshift range $1.7 < z < 4$ both from the literature as shown in the figure and our sample presented here. The errors in the $\tau_{\text{H I}}^{\text{eff}}$ measurements are taken into account in the fit. Despite the different method of measuring $\tau_{\text{H I}}^{\text{eff}}$, we also included the Kirkman et al. measurement. Note that the point at $z = 1.9$ by Tytler et al. (2004) is from low resolution data and is therefore not included in the fit. We did not include the Schaye et al. (2003) measurements from the spectra which are already included in our sample. The fit is given by $\tau_{\text{H I}}^{\text{eff}} = (0.0023 \pm 0.0007)(1+z)^{3.65 \pm 0.21}$. For our sample alone the power law is $\tau_{\text{H I}}^{\text{eff}} = (0.0054 \pm 0.0101)(1+z)^{2.96 \pm 0.83}$. This fit is shallower than that of the combined $\tau_{\text{H I}}^{\text{eff}}$ due to a small number of QSOs and a lack of high- z QSOs in our sample

⁹ There are several noticeable differences between the two $\tau_{\text{H I}}^{\text{eff}}$ measurements. Since the two $\tau_{\text{H I}}^{\text{eff}}$ values of the metal-included spectra are very similar, the difference is mainly caused by the incomplete metal removal in the Schaye et al. sample, i.e. their $\tau_{\text{H I}}^{\text{eff}}$ is somewhat larger. QSOs with more than 10% difference in $\tau_{\text{H I}}^{\text{eff}}$ are: J2233–606 at $1.732 < z < 1.963$ by $\sim 12\%$, Q0109–3518 at $1.874 < z < 2.120$ by $\sim 11\%$ and Q0002–422 at $2.434 < z < 2.710$ by $\sim 11\%$. In Fig. 13, the most noticeable is J2233–606, in part due to the fact that our redshift range used in this study differs from the one used by Schaye et al.

(cf. Kim et al. 2001; Kim et al. 2002). The dashed line is an extrapolated fit by Bernardi et al. (2003) to their low resolution, low signal-to-noise SDSS data (their $S/N > 4$ sample) in the redshift range $2.5 < z < 4$, while the dot-dot-dot-dashed line is a fit by Fan et al. (2006) to measurements at $3 < z < 5.5$ extrapolated to lower redshift, $\tau_{\text{H I}}^{\text{eff}} \propto (1+z)^{4.3 \pm 0.3}$. The slope of the power law evolution measured by Bernardi et al. is in good agreement within 1σ . As discussed extensively in the literature (e.g. Seljak et al. 2003; Viel et al. 2004b) there is, however, a systematic offset of about $\sim 25\text{--}30\%$ between the Bernardi et al. $\tau_{\text{H I}}^{\text{eff}}$ and our and other measurements from high-resolution, high S/N data. This is most likely attributable to the difficulty of continuum fitting for low resolution, low signal-to-noise data which appears to lead to a systematic overestimate of the effective optical depth. The Fan et al. measurement (the dot-dot-dot-dashed line) has a somewhat steeper redshift evolution. This might indicate that there is a deviation from a single power law at $z > 4$. Note that Becker, Rauch & Sargent (2007) have also argued that the redshift evolution at $z > 4$ steepens towards higher redshift and is not well fit by a power law anymore. At $1.7 < z < 4$, we find no evidence for a deviation from a power law. Table A5 in Appendix A lists the measurement of $\tau_{\text{H I}}^{\text{eff}}$ sampled at $\Delta z = 0.2$ as well as $\tau_{\text{H I}}^{\text{eff}}$ of each QSO belonging to each redshift bin.

6 CONCLUSIONS

We have obtained improved measurements of the flux probability distribution at $1.7 < z < 3.2$ and effective optical depth due to the intergalactic H I absorption at $1.7 < z < 4$, based on a sample of 18 high resolution, high signal-to-noise VLT/UVES QSO absorption spectra for which we have performed an extensive Voigt profile analysis of the H I and metal absorption.

The main results are as follows:

(i) The normalised flux probability distribution (PDF) is affected mainly by metals at the level of 10–20% at flux levels of $0.2 < F < 0.8$ depending on redshift, and by continuum fitting uncertainties at the level of 5–20% at flux levels of $0.8 < F < 1$, depending on the signal-to-noise of the spectra. The effects of pixel noise and zero-level offset are very small, only noticeable at $F \sim 0$ and $F \sim 1$. The metal contribution to the absorption varies from a few percent to up to 30 percent between different lines of sight. A careful individual removal of the metal absorption is therefore essential for an accurate determination of the shape of the PDF.

(ii) Our new measurements of the flux PDF due to H I alone are systematically lower at $0.2 < F < 0.7$ than the widely-used PDFs measured by McDonald et al. (2000) based on a sample of Keck/HIRES spectra half the size of our sample. The difference has the same sign as would be expected if the removal of the metal absorption by McDonald et al. (2000) was less complete than ours, but it is actually somewhat larger and does not have the correct redshift dependence if this were the sole cause. Given the rather small sample size cosmic variance is likely to be responsible for part of the discrepancy.

(iii) The effect of our improved removal of metal absorption on the measured effective optical depth due to H I absorption, compared to previous measurements where

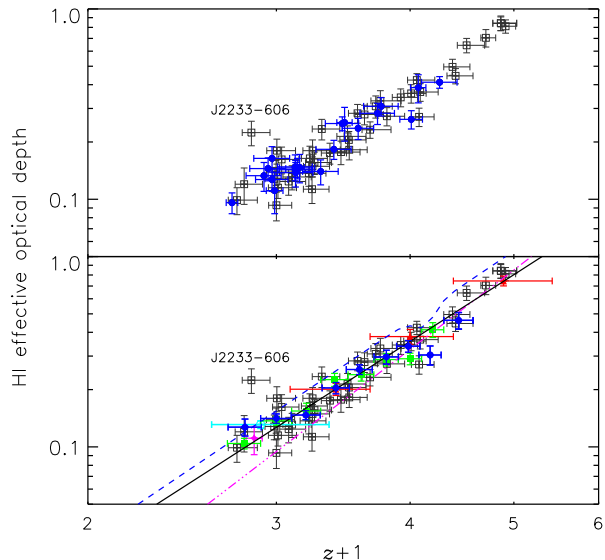


Figure 13. Comparison of the evolution of the effective optical depth of our full sample after removal of the metal absorption (filled circles) with that measured in Schaye et al. (2003, grey open squares). There is a large overlap in the two samples and as expected the estimates from the two studies are in good agreement (for J2233–606, see text). The horizontal and vertical error bars show the redshift range used and the 1σ errors. The errors were estimated using 500 bootstrap realisations of chunks of spectra with 100 pixels. The lower panel shows a comparison of the evolution of the effective optical depth of our sample divided into redshift bins with width $\Delta z = 0.2$ (filled circles with errors) to a compilation of other measurements from the literature. The open squares are the measurements of Schaye et al. (2003) as in the upper panel. The filled squares, the filled triangles, the filled diamond at $z = 1.86$, and the open circle at $z = 1.9$ are from Kirkman et al. (2005), McDonald et al. (2000), Janknecht et al. (2006) and Tytler et al. (2004), respectively. The solid line is the best fit to all high-resolution data in the figure both from the literature and the current sample in the redshift range $1.7 < z < 4$: $\tau_{\text{H I}} = (0.0023 \pm 0.0007)(1+z)^{3.65 \pm 0.21}$. The dashed curve is a fit from Bernardi et al. (2003) to their $S/N > 4$ SDSS data in the redshift range from $2.5 < z < 4$ extrapolated to lower redshift. The dot-dot-dot-dashed line is a fit by Fan et al. (2006) to data in the redshift range $3 < z < 5.5$ extrapolated to lower redshift.

the metal absorption has been taken into account in simpler ways, is small. Our new measurements of $\tau_{\text{H I}}^{\text{eff}}$ are in good agreement with other measurements from high resolution, high signal-to-noise spectra. In the redshift range $1.7 < z < 4$ the redshift evolution of the of our measurements of the effective optical depth and other measurements from high resolution spectra is best fit with a single power law $\tau_{\text{H I}}^{\text{eff}} = (0.0023 \pm 0.0007)(1+z)^{3.65 \pm 0.21}$.

ACKNOWLEDGMENTS.

We would like to thank ESO, the ESO staff, the ESO science verification team and the UVES LP team of “The cosmic evolution of the intergalactic medium” for initiating, compiling and making publicly available a superb set of QSO absorption spectra. We also thank the UVES team for building

the spectrograph and our referee Michael Strauss for his useful suggestions. TSK would like to thank Michael Murphy for providing his spectral combining program, UVES_popler, and the IoA, Cambridge, UK, for hospitality during the final stages of this work.

REFERENCES

- Becker G., Rauch M., Sargent W. L. W., 2007, *ApJ*, 662, 72
- Bergeron J., Petitjean P., Aracil B. et al., 2004, *Msngr*, 118, 40
- Bernardi M., Sheth R. K., SubbaRao M. et al., 2003, *AJ*, 125, 32
- Bolton J. S., Haehnelt M. G., Viel M., Springel V., 2005, *MNRAS*, 357, 1178
- Bryan G. L., Machacek M. E., Anninos P., Norman M. L., 1999, *ApJ*, 517, 13
- Carswell R.F., Schaye J., Kim T.-S., 2002, *ApJ*, 578, 43
- Cen R., Miralda-Escudé J., Ostriker J. P., Rauch M., 1994, *ApJ*, 437, L9
- Cowie L. L., Songaila A., Kim T.-S., Hu E. M., 1995, *AJ*, 109, 1522
- Cristiani S., D’Odorico V., 2000, *AJ*, 120, 1648
- Croft R. A. C., Weinberg D. H., Katz N., Hernquist L., 1998, *ApJ*, 495, 44
- Croft R.A.C., Weinberg D. H., Bolte M., Burles S., Hernquist L., Katz N., Kirkman D., Tytler D., 2002, *ApJ*, 581, 20
- Davé R., Hernquist L., Katz N., Weinberg D. H., 1999, *ApJ*, 511, 521
- Dekker H., D’Odorico S., Kaufer A., Delabre B., Kotzłowski H., 2000, *Proc. SPIE*, 4008, 534
- Desjacques V. & Nusser A., 2005, *MNRAS*, 361, 1257
- Desjacques V., Nusser A., Sheth R. K., 2007, *MNRAS*, 374, 206
- Fan X., Strauss M. A., Becker R. H. et al., 2006, *AJ*, 132, 117
- Fechner C., Baade R., Reimers D., 2004, *A&A*, 418, 857
- Hu E. M., Kim T.-S., Cowie L. L., Songaila A., Rauch M., 1995, *AJ*, 110, 1526
- Janknecht E., Reimers D., Lopez S., Tytler D., 2006, *A&A*, 458, 427
- Jena T., Norman M. L., Tytler D. et al., 2005, *MNRAS*, 361, 70
- Jenkins E. B. & Ostriker J. P., 1991, *ApJ*, 376, 33
- Kim T.-S., Cristiani S., D’Odorico S., 2001, *A&A*, 373, 757
- Kim T.-S., Carswell R. F., Cristiani S., D’Odorico S., Giallongo E., 2002, *MNRAS*, 335, 555
- Kim T.-S., Viel M., Haehnelt M. G., Carswell R. F., Cristiani S., 2004, *MNRAS*, 347, 355
- Kirkman D., Tytler D., 1997, *ApJ*, 484, 672
- Kirkman D., Tytler D., Suzuki, N. et al., 2005, *MNRAS*, 360, 1373
- Lesgourgues J., Viel M., Haehnelt M.G., Massey R., 2007, submitted, *astro-ph/07050533*
- Lidz A., Heitmann K., Hui L., Habib S., Rauch M., Sargent W. L. W., 2006, *ApJ*, 638, 27
- Lu L., Sargent W. L. W., Womble D. S., Takada-Hidai M., 1996, *ApJ*, 472, 509
- McDonald P., Miralda-Escudé J., Rauch M., Sargent W.L., Barlow T.A., Cen R., Ostriker J.P., 2000, *ApJ*, 543, 1
- McDonald P., Seljak, U., Burles S. et al., 2006, *ApJS*, 163, 80
- Meiksin A., Bryan G. & Machacek M., 2001, *MNRAS*, 327, 296
- Miralda-Escudé J., Cen R., Ostriker J. P., Rauch M., 1996, *ApJ*, 471, 58
- Morton D. C., 2003, *ApJS*, 149, 205
- Press W. H., Rybicki G. B., Schneider D. P., 1993, *ApJ*, 414, 64
- Rauch M., Miralda-Escudé J., Sargent W. L. W., Barlow T. A., Weinberg D. H., Hernquist L., Katz N., Cen R., Ostriker J. P., 1997, *ApJ*, 489, 7
- Schachter J., 1991, *PASP*, 103, 457
- Schaye J., Aguirre A., Kim T.-S., Theuns T., Rauch R., Sargent W. L. W., 2003, *ApJ*, 301, 478
- Seljak U., McDonald P., & Makarov A., 2003, *MNRAS*, 342, L79
- Songaila A., 2004, *AJ*, 127, 2598
- Theuns T., Leonard A., Efstathiou G., Pearce F. R., Thomas P. A., 1998, *MNRAS*, 301, 478
- Theuns T., Schaye J., Haehnelt M. G., 2000, *MNRAS*, 215, 600
- Tytler D. & Fan X.-M., 1992, *ApJS*, 79, 1
- Tytler D., Kirkman D., O’Meara J. M. et al., 2004, *ApJ*, 617, 1
- Vanden Berk D. E., Richards G. T., Bauer, A., et al., 2001, *AJ*, 122, 549
- Viel M., Haehnelt M. G., Carswell R.F., Kim T.-S., 2004a, *MNRAS*, 349, L33
- Viel M., Haehnelt M. G., Springer V., 2004b, *MNRAS*, 354, 684
- Viel M., Haehnelt M. G. & Lewis A., 2006, *MNRAS*, 370, 51
- Weinberg D. H., Burles S. Croft R. A. C. et al., 1998, in *Evolution of Large Scale Structure: From Recombination to Garching*, eds. A. J. Banday, R. K. Sheth & L. N. Da Costa (Twin Press: Vledder NL), p. 346
- Zhang Y., Anninos P., Norman M. L., Meiksin, A., 1997, *ApJ*, 485, 496

Table A1. The wavelength range of each spectrum in the three redshift bins

QSO	$\langle z \rangle = 2.07$	$\langle z \rangle = 2.52$	$\langle z \rangle = 2.94$
Q0055–269			4785–5112
PKS2126–158			4638–5112
Q0420–388		4231–4506	4506–4909
HE0940–1050		4197–4502	4502–4870
HE2347–4342		4055–4502	4502–4643
Q0002–422	3901–4092	4092–4504	
PKS0329–255	3815–4090	4090–4439	
Q0453–423		4084–4362	
HE1347–2457	3705–4091	4091–4319	
Q0329–385	3528–4105		
HE2217–2818	3509–4091		
Q0109–3518	3532–4070		
HE1122–1648	3514–4082		
J2233–606	3335–3886		
PKS0237–23	3361–3865		
PKS1448–232	3306–3860		
Q0122–380	3306–3819		
Q1101–264	3503–3765		

APPENDIX A: TABLES

Table A2. Uncertain line fits for individual QSOs^a

QSO	Uncertain line fits
Q0055–269	Si III at $z = 3.2562$ (m), Si II 1260 at $z = 3.2562$ (l)
PKS2126–158	Si II 1260 at $z = 2.9071$ (l), Si III at $z = 2.9067$ (m), Si III at $z = 2.7668$ (m)
Q0420–388	Si III 1260 at $z = 2.5372$ (l), Si IV 1394 at $z = 2.2475$ (l), Si IV 1403 at $z = 2.2475$ (l)
HE0940–1050	Si II 1260 at $z = 2.8346$ (l), C II 1334 at $z = 2.3306$ (l), O I 1302 at $z = 2.3292$ (l), C II 1334 at $z = 2.2212$ (m)
HE2347–4342	Si III at $z = 2.7412$ (m), Si II 1260 at $z = 2.3124$ (l)
Q0002–422	Si II 1260 at $z = 2.4623$ (l), Si III at $z = 2.4642$ (m), Si III at $z = 2.3022$ (m)
PKS0329–255	Si III at $z = 2.3289$ (m)
Q0453–423	Al II at $z = 1.6172$ (l)
HE1347–2457	C IV 1548 at $z = 1.6083$ (m)
Q0329–385	
HE2217–2818	Si III at $z = 1.9653$ (l), C II 1334 at $z = 1.690983$ (l)
Q0109–3518	C II 1334 at $z = 2.0463$ (m), Si III at $z = 2.0473$ (l)
HE1122–1648	Si III at $z = 2.0071$ (m)
J2233–606	Si III at $z = 1.9426$ (h), Si III at $z = 1.9257$ (m) Si III at $z = 1.8711$ (m), C II 1334 at $z = 1.8711$ (l)
PKS0237–23	C IV 1548, 1550 at 1.3643 (m), Si III at $z = 2.1781$, C II 1334 at $z = 1.6756$ (m), C II 1334 at $z = 1.6359$ (m)
PKS1448–232	C II 1334 at $z = 1.5855$ (l)
Q0122–380	Si III at $z = 1.9733$ (m), Si II 1260 at $z = 1.9695$ (l), Si III at $z = 1.9123$ (l), Si III at $z = 1.9102$ (m)
Q1101–264	

^a The letters “m” and “l” indicate a “moderate” uncertainty and a “low” uncertainty, respectively. For the class “l” the H I profiles do not change significantly with and without the uncertain metal lines (*cf.* Si II 1260 in Fig. 3 f). The example of the Si III absorption in Fig. 3 f) is a typical uncertain line fit of class “m”.

Table A3. The mean PDF of the full sample divided into three and two redshift bins.

F	$\langle z \rangle = 2.07$	$\langle z \rangle = 2.52$	$\langle z \rangle = 2.94$	$\langle z \rangle = 2.41^a$	$\langle z \rangle = 3.00^a$
0.00	0.5700± 0.0581	0.9189± 0.0995	1.6960± 0.2043	0.8009± 0.1114	1.6277± 0.2356
0.05	0.1978± 0.0165	0.3540± 0.0320	0.4666± 0.0520	0.2870± 0.0362	0.4861± 0.0603
0.10	0.1354± 0.0115	0.2426± 0.0190	0.2957± 0.0312	0.1851± 0.0227	0.3210± 0.0396
0.15	0.1401± 0.0098	0.2064± 0.0199	0.2799± 0.0281	0.1664± 0.0215	0.2950± 0.0371
0.20	0.1230± 0.0083	0.1873± 0.0151	0.2356± 0.0230	0.1624± 0.0172	0.2574± 0.0330
0.25	0.1307± 0.0078	0.2230± 0.0206	0.2403± 0.0212	0.1822± 0.0177	0.2412± 0.0291
0.30	0.1216± 0.0086	0.2003± 0.0168	0.2385± 0.0197	0.1630± 0.0141	0.2350± 0.0230
0.35	0.1279± 0.0083	0.1995± 0.0151	0.2310± 0.0198	0.1517± 0.0135	0.2323± 0.0273
0.40	0.1450± 0.0088	0.2151± 0.0133	0.2502± 0.0195	0.1941± 0.0146	0.2646± 0.0283
0.45	0.1488± 0.0083	0.2574± 0.0196	0.2496± 0.0166	0.1907± 0.0147	0.2448± 0.0188
0.50	0.1726± 0.0099	0.2561± 0.0180	0.2817± 0.0195	0.2162± 0.0198	0.2717± 0.0265
0.55	0.1884± 0.0104	0.2800± 0.0170	0.3523± 0.0201	0.2462± 0.0207	0.3480± 0.0235
0.60	0.2209± 0.0114	0.3323± 0.0206	0.4246± 0.0228	0.3158± 0.0285	0.4009± 0.0247
0.65	0.2815± 0.0144	0.3588± 0.0195	0.4555± 0.0351	0.3702± 0.0306	0.4269± 0.0297
0.70	0.3067± 0.0136	0.4107± 0.0183	0.5785± 0.0342	0.4154± 0.0254	0.5793± 0.0432
0.75	0.4045± 0.0170	0.5631± 0.0284	0.6888± 0.0485	0.5417± 0.0362	0.7354± 0.0582
0.80	0.5747± 0.0239	0.8030± 0.0358	0.9168± 0.0587	0.7511± 0.0513	0.9470± 0.0713
0.85	0.8440± 0.0317	1.1532± 0.0712	1.4003± 0.0660	1.0816± 0.0731	1.4178± 0.0733
0.90	1.6501± 0.0464	2.0285± 0.1072	2.1911± 0.0841	2.0036± 0.1064	2.1899± 0.0929
0.95	4.9083± 0.0982	4.6174± 0.1175	3.9641± 0.1729	4.9196± 0.1604	3.9674± 0.1805
1.00	8.6081± 0.1986	6.1926± 0.3069	4.5630± 0.3659	6.6550± 0.3420	4.5108± 0.4290

^a The wavelength ranges for $\langle z \rangle = 2.41$ and $\langle z \rangle = 3.00$ are 3902–4325 Å (5 QSOs: HE2347–4342, Q0002–422, PKS0329–255, Q0453–423 and HE1347–2457), and 4703–5112 Å (4 QSOs: Q0055–269, PKS2126–158, Q0420–388 and HE0940–1050), respectively.

Table A4. The H I effective optical depth^a

QSO	wavelengths (Å)	$\langle z \rangle$	$\tau_{\text{H I}}^{\text{eff}}$	$\overline{F}_{\text{H I}}$	σ_F^2	$\tau_{\text{H I}+\text{metal}}^{\text{eff}}$	Metals (%)
Q0055–269	4785–5577	3.262	0.412 \pm 0.029	0.662 \pm 0.020	0.1233 \pm 0.0065	0.419 \pm 0.030	1.6
	4785–5112	3.071	0.386 \pm 0.046	0.680 \pm 0.033	0.1296 \pm 0.0119	0.388 \pm 0.046	0.5
PKS2126–158	4638–5112	3.010	0.263 \pm 0.025	0.769 \pm 0.019	0.0949 \pm 0.0086	0.351 \pm 0.031	25.0
Q0420–388	4231–4909	2.759	0.308 \pm 0.024	0.735 \pm 0.017	0.1092 \pm 0.0068	0.332 \pm 0.025	7.2
HE0940–1050	4197–4870	2.729	0.283 \pm 0.023	0.754 \pm 0.018	0.1004 \pm 0.0086	0.325 \pm 0.025	13.0
HE2347–4342	4055–4643	2.577	0.236 \pm 0.022	0.790 \pm 0.018	0.0900 \pm 0.0092	0.241 \pm 0.022	2.3
Q0002–422	3901–4504	2.457	0.250 \pm 0.021	0.778 \pm 0.016	0.0912 \pm 0.0081	0.325 \pm 0.025	23.1
PKS0329–255	3815–4439	2.395	0.183 \pm 0.020	0.833 \pm 0.015	0.0762 \pm 0.0088	0.196 \pm 0.020	6.4
Q0453–423	4084–4362	2.474	0.253 \pm 0.031	0.777 \pm 0.024	0.0904 \pm 0.0113	0.271 \pm 0.033	6.7
	3758–3911	2.154	0.147 \pm 0.026	0.864 \pm 0.022	0.0523 \pm 0.0110	0.161 \pm 0.025	9.0
HE1347–2457	3705–4319	2.300	0.140 \pm 0.015	0.870 \pm 0.013	0.0544 \pm 0.0079	0.165 \pm 0.016	15.4
Q0329–385	3528–4105	2.139	0.146 \pm 0.013	0.864 \pm 0.012	0.0543 \pm 0.0066	0.150 \pm 0.013	2.7
HE2217–2818	3509–4091	2.126	0.138 \pm 0.014	0.871 \pm 0.014	0.0557 \pm 0.0076	0.168 \pm 0.016	17.8
Q0109–3518	3532–4070	2.127	0.143 \pm 0.015	0.867 \pm 0.014	0.0590 \pm 0.0078	0.168 \pm 0.016	14.7
HE1122–1648	3514–4082	2.124	0.148 \pm 0.017	0.863 \pm 0.014	0.0603 \pm 0.0079	0.161 \pm 0.017	8.0
J2233–606	3350–3886	1.976	0.164 \pm 0.019	0.849 \pm 0.017	0.0707 \pm 0.0106	0.179 \pm 0.019	8.4
PKS0237–23	3361–3865	1.972	0.127 \pm 0.015	0.880 \pm 0.013	0.0527 \pm 0.0077	0.176 \pm 0.019	27.6
PKS1448–232	3306–3860	1.947	0.145 \pm 0.014	0.865 \pm 0.013	0.0604 \pm 0.0071	0.157 \pm 0.014	7.6
Q0122–380	3282–3819	1.921	0.133 \pm 0.018	0.875 \pm 0.015	0.0613 \pm 0.0096	0.160 \pm 0.019	16.4
Q1101–264	3503–3765	1.989	0.111 \pm 0.021	0.895 \pm 0.018	0.0435 \pm 0.0098	0.129 \pm 0.022	14.1
	3233–3398	1.727	0.096 \pm 0.020	0.908 \pm 0.018	0.0316 \pm 0.0110	0.131 \pm 0.026	26.9

^a The errors were estimated using 500 bootstrap realisations of chunks of 100 pixels (5 Å).**Table A5.** The evolution of the effective optical depth of the full sample divided into redshift bins with width $\Delta z=0.2^a$

$\langle z \rangle$	Wavelengths (Å)	$\tau_{\text{H I}}^{\text{eff}}$	$\langle z \rangle$	Wavelengths (Å)	$\tau_{\text{H I}}^{\text{eff}}$
1.80	3282–3525	0.127 \pm 0.013	2.41	4012–4255	0.204 \pm 0.015
	J2233–606	0.203 \pm 0.039		HE2347–4342	0.156 \pm 0.022
	PKS0237–23	0.111 \pm 0.024		Q0002–422	0.228 \pm 0.034
	PKS1448–232	0.126 \pm 0.022		PKS0329–255	0.186 \pm 0.034
	Q0122–380	0.097 \pm 0.018		Q0453–423	0.252 \pm 0.042
	Q1101–264	0.095 \pm 0.027		HE1347–2457	0.205 \pm 0.022
2.00	3525–3769	0.141 \pm 0.008	2.59	4255–4498	0.255 \pm 0.016
	Q0329–385	0.128 \pm 0.017		Q0420–388	0.266 \pm 0.031
	HE2217–2818	0.133 \pm 0.023		HE0940–1050	0.293 \pm 0.033
	Q0109–3518	0.156 \pm 0.026		HE2347–4342	0.258 \pm 0.022
	HE1122–1648	0.117 \pm 0.019		Q0002–422	0.268 \pm 0.034
	J2233–606	0.168 \pm 0.039		PKS0329–255	0.170 \pm 0.037
	PKS0237–23	0.146 \pm 0.022		Q0453–423	0.255 \pm 0.060
	PKS1448–232	0.157 \pm 0.021	2.80	4498–4741	0.297 \pm 0.024
	Q0122–380	0.165 \pm 0.017		PKS2126–158	0.231 \pm 0.052
	Q1101–264	0.098 \pm 0.021		Q0420–388	0.308 \pm 0.034
2.20	3769–4012	0.147 \pm 0.009		HE0940–1050	0.304 \pm 0.033
	Q0002–422	0.269 \pm 0.046		HE2347–4342	0.315 \pm 0.025
	PKS0329–255	0.191 \pm 0.036	2.99	4741–4984	0.338 \pm 0.024
	Q0453–423	0.142 \pm 0.022		Q0055–269	0.389 \pm 0.062
	HE1347–2457	0.094 \pm 0.021		PKS2126–158	0.310 \pm 0.044
	Q0329–385	0.138 \pm 0.017		Q0420–388	0.380 \pm 0.038
	HE2217–2818	0.152 \pm 0.022		HE0940–1050	0.260 \pm 0.046
	Q0109–3518	0.127 \pm 0.027	3.18	4984–5227	0.304 \pm 0.035
	HE1122–1648	0.163 \pm 0.019		Q0055–269	0.362 \pm 0.050
	J2233–606	0.096 \pm 0.019		PKS2126–158	0.203 \pm 0.059
			3.44 ^b	Q0055–269	0.462 \pm 0.045

^a The errors were estimated using 500 bootstrap realisations of chunks of 100 pixels (5 Å). For each bin, $\tau_{\text{H I}}^{\text{eff}}$ was estimated from the mean flux of all pixels from the QSOs listed.^b Q0055–269 is the only QSO in this z bin.